NASA TECHNICAL MEMORANDUM NASA TM-88530

PROCEDURE FOR COMPUTING TRANSSONIC FLOWS FOR CONTROL OF ADAPTIVE WIND TUNNELS

Rainer Rebstock

Translation of: "Verfahren Zur Berechnung Transsonischer Stromungen Fur Die Regelung Adaptiver Windkanale," dissertation presented Vom Fachbereich Verkehrswen der Technischen Universitat Berlin, (Mar.) 1986

NATIONAL AERONAUTICS AND SPACE ADMINISTRATION
WASHINGTON, D.C. 20546 JANUARY 1987

STANDARD TITLE PAGE

1. Report No.	2. Government Accession No.	3. Recipient's Catalog No.
NASA TM-88530		

4. Title and Subtitle	5. Report Date
PROCEDURE FOR COMPUTING TRANSSONIC FLOWS FOR CONTROL OF ADAPTIVE WIND TUNNELS	JANUARY 1987
	6. Performing Organization Code

7. Author(s)	8. Performing Organization Report No.
Rainer Rebstock	
	10. Work Unit No.

9. Performing Organization Name and Address	11. Contract or Grant No.
SCITRAN Box 5456 Santa Barbara, CA 93108	NASw- 4004
	13. Type of Report and Period Covered
	Translation
12. Sponsoring Agency Name and Address	14. Sponsoring Agency Code
National Aeronautics and Space Administration Washington, D.C. 20546	

15. Supplementary Notes

Translation of: "Verfahren Zur Berchnung Transsonischer Stromungen Fur Die Regelung Adaptiver Windkanale," dissertation presented Vom Fachbereich Verkehrswen der Technischen Universitat Berlin, (Mar.) 1986

16. Abstract

In this work, numerical methods are developed for control of three-dimensional adaptive test sections. The physical properties of the design problem occurring in the external field computation are analyzed, and a design procedure suited for solution of the problem is worked out. To do this, the desired wall shape is determined by stepwise modification of an initial contour. The necessary changes in geometry are determined with the aid of a panel procedure, or, with incident flow near the sonic range, with a TSP procedure.

17. Key Words (Selected by Author(s))	18. Distribution Statement
	Unclassified and Unlimited

19. Security Classif. (of this report)	20. Security Classif. (of this page)	21. No. of Pages	22. Price
Unclassified	Unclassified	108	

TM88530(1229-116)

PROCEDURE FOR COMPUTING TRANSSONIC FLOWS FOR CONTROL OF ADAPTIVE WIND TUNNELS

Presented by
Graduate Mathematician
Rainer Rebstock

Dissertation presented
from the Transportation Faculty of the
Berlin Technical College
toward the academic degree of
Doctor of Engineering

Date of oral examination: 24 March 1986

Berlin, 1986

Table of Contents:

SUMMARY

/1*

In this work, numerical methods are developed for control of three-dimensional adaptive test sections. The physical properties of the design problem occurring in the external field computation are analyzed, and a design procedure suited for solution of the problem is worked out. To do this, the desired wall shape is determined by stepwise modification of an initial contour. The necessary changes in geometry are determined with the aid of a panel procedure or, with incident flow near the sonic range, with a TSP procedure.

The poor convergence properties of the classical iterative adaptation process in the 3D case are demonstrated by means of a numerical simulation and a theoretical study. At the same time it is shown that by means of a simple replacement of the constant control factor by a matrix which considers the incident Mach number and test section geometry, computation of the adapted wall contour can be determined practically in one step, i. e., on the basis of a single wind tunnel test. The capability of this one-step method is demonstrated by means of measurements from the adaptive octagonal test section of the Berlin Technical College.

Finally, a new method is presented for testing three-dimensional models in wind tunnels with two flexible walls. Wall designs are presented by means of which the interferences on the model axis can be eliminated.

*Numbers in margin refer to foreign pagination.

This work was performed as part of the research project "Development of an adaptive wind tunnel test section with flexible walls for three-dimensional transsonic flows", supported by the Federal Ministry for Research and Technology.

1. SYMBOLS

(x,y,z)	
(ξ,η,ζ)	Cartesian coordinates /2
(x,r,θ)	Cylindrical coordinates
(x_p,y_p,z_p)	Coordinates of plotted point p
(x_q,y_q,z_q)	Coordinates of origin point q
(x_d,y_d,z_d)	Coordinates of wall pressure holes d
$\vec{x}^{>} = (x,y,z)$	Location vector
S, S_1	Control surface
B_i, Bereich I	Region within the control surfaces (near-model region)
B_e, Bereich II	Infinite region outside the control surfaces (external field)
n, n_A	External normal of S
I_u	Internal normal of S
x_A	Beginning of test section
x_E	End of test section
F_A	Initial cross section
F_E	Final cross section
$\bar{R}$	Mean wall distance from the tunnel axis for the j-th surface panel
Δ_j	Number of panels
N	Surface element
dF	Height of test section
h	Wall deflection
$h(x)$	Half-length of the basic wave (design rule)
L	Circular frequency
ω	Incident flow Mach number (uncorrected)
M_∞	Compressibility factor
$\beta = \sqrt{1-M_\infty^2}$	Incident flow velocity (uncorrected)
U_∞	Perturbing velocity potential (normalized with U_∞) /3
ϕ	

Octagon Test Section

$u = \frac{\partial \phi}{\partial x}$	Perturbing velocity in the x direction
$v = \frac{\partial \phi}{\partial n}$	Perturbing velocity normal to S
$U_{ges} = U_\infty + u$	Total axial velocity
$\delta\phi$	Additional potential (perturbation computation)
Ψ	Flow function
C_p	Pressure coefficient
C_A, C_L	Lift coefficient
C_w	Drag coefficient
C_{M25}	Pitch moment coefficient at 25% of the aerodynamic wing depth
κ	Ratio of specific heats
α	Model angle of incidence
$g(p,q)$	Compressible source potential
ζ, σ	Source strength
$A=(A_{ij})$	Influence coefficients (u-component)
$B=(B_{ij})$	Influence coefficients (v-component)
$A'=E-A$	Influence coefficients for internal flow
E	Unit matrix
K	Weighting factor in the iterative wall adaptation method
I_0, I_1, K_0, K_1	Modified Bessel functions
0	Landau symbol
ε	Tolerance magnitude

Indices:

w	wall-induced
∞	model-induced, interference-free
A	in the direction n_A
I	in the direction n_I
o	upper tunnel wall

u	lower tunnel wall
eff, kor	effective (incident flow)
D	design
E	design

design methods

Strokes above a value indicate averaging or transition to conjugated complexes.

2. INTRODUCTION

/5

In a wind tunnel, the flow field must satisfy a kinematic boundary condition along the test section wall, in contrast to a laterally inbounded flow around a model. For instance, in test sections with impermeable walls the course of the flow lines near the wall is determined solely by the wall contour. The flow lines in the wall region, therefore, do not generally correspond to those which would be there with free flow around the model. This leads to interferences in the whole test section flow and introduces errors into the aerodynamic data measured with the model.

The wall-induced perturbation velocity field is normally very complex, but it can be at least approximately represented as a superimposition of various independent effects. The two most important of these are the axial additional velocity (blocking) produced by the changed lateral bending of the flow lines in the region of the model, and the change in model lift due to the diversion of the downflow field at the tunnel walls (lift interference). For example, in test sections with flat impermeable walls the blocking effect leads to an increase of the effective incident flow velocity and, thus, of the stagnation pressure (in the subsonic region), while there is generally an increase in lift and therefore an increase of the effective model incidence angle. The measured data, with interferences, then as a first approximation describe the actual aerodynamic behavior of the model studied with somewhat altered incident flow conditions. Many numerical methods have been developed in the course of time for computing the corrections ΔM_∞ and $\Delta\alpha$.

For wind tunnel studies in the transsonic range, where the test section walls must be slotted or perforated to avoid the transsonic blocking, though, application of these correction methods encounters great difficulties. The boundary condition for partially permeable tunnel walls can only be approximately described mathematically, so that the corrections determined on the basis of this information (and a representation of the model investigated by means of suitable singularities) are likewise troubled with great uncertainties.

Furthermore, one must consider that the "global" consideration of the wall interferences in the form of the two incident flow parameters ΔM_∞ and $\Delta\alpha$, as described so far, is justified only if the wall-induced perturbation velocities are nearly constant in the region of the model. This is generally the case only with very small blocking ratios. On the other hand, in view of ability to transfer the model data measured in the wind tunnel to the full-scale design, one must certainly try to test the largest possible model (Reynolds number similarity). Because of the continuously increasing requirements in recent years for quality of wind tunnel measurements in the high subsonic region, the design of new test sections which can provide model measurements which are free of interferences, or at least correctable, with maintenance of a high blocking ratio, is becoming more and more pressing.

This requirement was the cause of the development of the so-called "adaptive" wind tunnels, which early in 1970 realized in design the obvious idea of eliminating the cause of the wall interferences by matching the test section walls to the laterally unbounded flow around the model. First, test sections with two adaptive walls were

produced for profile studies, based on highly developed computer and control technology. The adaption was produced either by deforming the flexible walls into free flight flow surfaces or, in the case of ventilated tunnels, by appropriate adjustment of the local wall permeability. The necessary displacement of the test section walls or the adjustment of their porosity must be completely automatic to have short test times. For this, it was necessary to solve basic design and control technology problems.

Furthermore, application of this new wind tunnel technology would be promising only after a practical method had been found for determining the adapted wall shape (see Chapter 3). That is, direct calculation of the free flight flow surfaces would be very costly because of the normally complex model geometry and the friction and compressibility effects which occur, and it would not be possible with sufficient accuracy, especially in the transsonic speed range.

Testing of the 2D adaptive test sections using some standard profiles (NACA ØØ12, CAST7) categorically confirmed that wall adaptation could be done practically, thus justifying the added design and electronic cost. On the basis of this great success, design of three-dimensional adaptive wind tunnels was begun in 1979. Of the three designs which have been realized so far, the test section with eight flexible walls, constructed at the Berlin Technical College, is described in more detail in the 4th section.

The principal objective of this work, though, is presentation of the numerical methods developed at the Berlin Technical College for three-dimensional wall adaptation. Initially, we shall consider generally the functional principle of adaptive wind tunnels for determining the adapted wall shape.

3. PHYSICAL FUNDAMENTALS OF THE TECHNOLOGY OF ADAPTIVE WIND TUNNELS

/8

The basic functional principle of adaptive wind tunnels was developed by Ferri and Baronti [1] and by Sears [2]. By comparing the tunnel flow with the laterally unbounded flow around the model they were successful in stating an analytic relation by means of which one can determine the wall interferences in the test section without explicit knowledge of the model being investigated. Derivation of this relation and of the iterative wall adaptation process based on it is carried out in the following for the general case of three-dimensional flows.

An important point of view here is the division of the laterally unbounded flow field (initially seeming rather arbitrary) into a region near the model and the so-called far- or external field. In Figure 1 these two flow regions, which fuse into each other, are delimited by an imaginary control surface. Within the control surface (region I) the flow field is very complex for the reasons already stated, and can only be approximated with the presently known computation methods. In the infinitely extended exterior field (region II), though, the model-induced perturbations have already decayed sufficiently, at sufficiently great lateral distance, that the flow here can be considered free of rotation, and the perturbation velocity potential can be matched to a good approximation by a simple differential equation. Experience has shown that the linearized potential equation, or its transsonic variant, is sufficient for this.

Approximation of the far field by a potential flow now leads immediately to an analytical criterion for freedom from interference. On the basic of mathematical uniqueness rules (see, for instance, [3]) the velocity potential is already unambiguously determined if along with the condition of vanishing perturbations at infinity, either the model-induced perturbation velocity in the incident flow or in the normal direction on the control surface S is specified. (S can initially be considered as infinitely long.) If one calculates the perturbation velocity potential ϕ with the u-component as a boundary condition on the control surface $\frac{\partial \phi}{\partial x}(S) = u(S)$, then the matching normal velocity follows from differentiation $v_A[u] = \frac{\partial \phi}{\partial n}(S)$ and conversely. With laterally unbounded flow around the model, the perturbation velocity components on the control surface then fulfill a compatibility relation which can be evaluated analytically.

By means of this criterion one can now determine easily whether a wind tunnel flow is interference-free, and if necessary undertake an adjustment of the adaptive test section walls. For this we measure two independent velocity components, e. g., the u- and v-flow on the control surface which is now assumed to be in the test section. If both these measured velocities fulfill the compatibility relation above, then the flow around the model in the tunnel can be expanded continuously to a laterally unbounded flow field, and it is therefore interference-free. Conversely, an interference-free tunnel flow can be considered part of an unbounded flow field, so that the equation derived above applies for the velocity components on the control surface. If we designate the measured u- and v-flows as $u_I(S)$ and $v_I(S)$, then the flow in the test section is exactly interference-free if the relation

$$v_A\,[u_I] = v_I \qquad (3.1)$$

applies on the control surface.

But if the calculated normal velocity v_A on the control surface, for flow around the model which is considered to be extended laterally without limit, is not identical with the corresponding measured component v_I, $v_A(S) - v_I(S) \neq 0$, then the tunnel flow has interferences and correction using the adaptive test section walls is necessary.

The difference, $v_A(S) - v_I(S)$ is obviously a measure of the magnitude of the wall interferences, and it therefore appears reasonable to adjust the contour or the porosity of the tunnel walls so as to produce an averaged (with a weighting factor K) normal velocity distribution on the control surface:

$$v_I^{new} = v_I + K(v_A - v_I), \quad K\varepsilon(0,1) \qquad (3.2)$$

Now the resulting tangential velocity $u_I^{new}(S)$ is measured and another test made by means of an external field computation to see whether the flow field within the control surface already matches that for laterally unlimited flow around the model. The difference, $v_A[u_I^{new}] - v_I^{new}$ is again used to correct the adaptive test section walls, and the entire process is repeated until the wall-induced flows have become negligibly small.

In summary, we have the following iteration scheme for wall adaptation, Figure 2:

$$v_A^{(n)} = v_A[u_I^{(n)}] \qquad \text{external field calculation} \quad n=1,2\ldots$$

$$v_I^{(n+1)} = v_I^{(n)} + K(v_A^{(n)} - v_I^{(n)}),\ K\varepsilon(0,1) \qquad (3.3)$$

The tunnel flow is considered to be interference-free if the change of the v-component in two successive iteration steps, and thus the correction of the adjusted wall configuration, remains within a specified tolerance $\varepsilon>0$.

$$|v_I^{(n+1)} - v_I^{(n)}| < \varepsilon \qquad (3.4)$$

One should consider that use of the adaptation process (3.3) provides no direct information about the model being investigated, and is therefore universally useful. The complex flow field within the test section is represented only by two independent flow quantities, such as the u- and v-perturbing velocities, along a control surface near the wall. Their repeated measurement along with the so-called external field calculation makes possible stepwise reduction of the wall interferences.

It must be emphasized, though, that the convergence properties of the control algorithm (3.3) depend strongly on the selection of the weighting or control factor K. As a result, there is a special practical importance to determination of an optimal value K_{opt} which leads to the adapted wall configuration with the fewest possible steps. Investigations of this sort are performed in Chapter 6 for three-dimensional wall adaptations. They show simultaneously how (3.3) must be modified with respect to rapid convergence (single-step method).

The numerical methods for the external field calculation required in each adaptation step are considered extensively in the 5th Chapter. In the following section we shall first explain the basic problems in the design of three-dimensional adaptive wind tunnels. Then the test section with eight flexible walls, built at the Berlin Technical College, is described in detail.

4. 3-D ADAPTIVE TEST SECTION AT THE BERLIN TECHNICAL COLLEGE

/13

In the design of three-dimensional adaptive test sections we could utilize the experimental results already gained with adaptive profile tunnels. Evaluation of the test results was particularly successful with respect to the practical feasibility of wall adaptation either with flexible impermeable walls or with ventilated test section walls.

The principle of partly permeable walls with locally controllable through-flow volumes (controlled either by variation of the wall porosity or by individual matching of the counterpressure in the sectionally divided plenum chambers) has been applied particularly in the USA. It appeared advantageous, especially economically, because the usual transsonic test sections are slotted or perforated, and could therefore be re-equipped relatively easily.

In comparison to the adaptive profile tunnels with flexible walls, built in Europe, this technique showed significant practical disadvantages from the beginning. This became particularly apparent in the measurement of the near-wall perturbation velocity distribution at both sides of the profile in the flow, required at each adaptation step. With impermeable walls, the two desired velocity components can be determined directly from the wall shape ($v = h'$) and the pressure distribution prevail ing there ($u = - Cp/2$). But with ventilated tunnels, measurements within the flow

field are necessary because of the severly inhomogeneous flow near the walls. These can, to be sure, be performed without contact by means of lasers, but this method is relatively time-consuming and is defensible only for adaptive profile tunnels.

The problem of rapid and precise measurement becomes more important in design of a three-dimensional adaptive test section because of the increased amount of data (longitudinal and normal perturbing velocity distribution along a control surface surrounding the model). It was principally for this reason that in Germany (at the Berlin Technical College and later at DFVLR, Göttingen) the decision was for design on the basis of impermeable, deformable walls [4]. (Other reasons were the higher power consumption and the higher noise level of ventilated test sections.)

At about the same time in the USA, though, work was started on construction of a three-dimensional adaptive tunnel with four ventilated walls [5]. A new kind of measuring system, which has become known as the "Calspan Pipe" was developed to determine the perturbing velocity components. It consists essentially of two metal tubes with static pressure holes, which can be turned about the longitudinal axis of the wind tunnel model, Figure 3. To be sure, experience so far has not been satisfactory. That, along with other problems, has as yet prevented a convincing functional demonstration of this test section [6].

In contrast, it has been possible to carry out initial successful wall adaptations with the two other 3D adaptive test sections, and to demonstrate the general applicability of the technique, which has in the meantime been established

for profile studies, for three-dimensional flow cases as well (see Chapter 9). The so-called "extensible adaptive test sections" built by the DFVLR in Göttingen is described in [7] along with the most important experimental results. In the following we shall consider the design details of the test system developed at the Berlin Technical College.

Design of the test section began with the basic idea that an ideal three-dimensional wall adaptation is hardly achievable in design, and not achievable at all at least for subsonic flows. Important viewpoints for the design, then, were the provision of the least possible mechanical cost while simultaneously providing adequate deformability of the test section walls. This compromise which was attempted led finally to design of the "octagon" test section with eight flexible walls [8].

Figure 4 shows the octagonal test section cross section formed from the eight walls and the layers between them (the model is described in Chapter 9). The principal dimensions (height 15 cm, width 18 cm) were chosen in the ratio of 1:1.2 with respect to a planned full-scale "European Transsonic Wind Tunnel", ETW. The test section length of 83 cm arises from the dimensions of the connections to the Technical College wind tunnel. Each flexible wall is individually deformable by means of 10 positioning elements in each (9 in the upper and lower walls), positioned longitudinally. The deformation and position control are fully automatic [8]. Figure 5 is an outer view of the test section showing the arrangement of the positioning motors. The wall pressure distribution is measured by a total of 192 (6 x 25; 2 x 21) pressure holes along the center lines of the flexible walls.

It was practical to choose the flow tube formed by the straight, undeformed test section walls as the control surface for the external field calculation (see Chapter 3). (Selection of a fixed interation-independent control surface is important for performing the adaptation quickly.) The perturbation velocity components needed there can be taken unchanged from the wall measurements because of the expected small contour changes. (The effect of the wall boundary layer is considered approximately by calibration of the empty test section, Chapter 9.2.)

The next sections describe extensively the numerical methods developed for the external field calculation.

5. NUMERICAL PEFORMANCE OF THE EXTERNAL FIELD COMPUTATION

5.1 Basic Comments

/17

The boundary value problem to be solved in the external field computation is, using the "theory of small disturbances" (Chapter 3), Figure 6:

$$(1-M_\infty^2)\phi_{xx} + \phi_{yy} + \phi_{zz} = \begin{cases} 0 & \text{subsonic} \quad (a) \\ (\kappa+1)\, M_\infty^2 \phi_x \phi_{xx} & \text{transsonic} \quad (b) \end{cases}$$

$$\phi(\vec{x}) = \int_{-\infty}^{x} u_I(t,y,z)\,dt \quad , \quad \vec{x} \in S \qquad (5.1)$$

$$\phi = 0\left(\frac{1}{|\vec{x}|}\right), \qquad |\vec{x}| \to \infty$$

We seek the normal perturbation velocity components $v_A[u_I] = \frac{\partial \phi}{\partial n}$ on the control surface S. Clearly explained, this is a matter of calculating that wall shape which would experience the measured pressure distribution in the fictive external flow.

Then the (unfavorable) physical properties of this three-dimensional design problem are demonstrated by means of a singularity representation for the solution in subsonic flow. In the next chapter we then present the design method supported by computation developed for this purpose.

We generate the desired potential by a source-sink distribution over the control surface. (Sources and sinks are preferred to a dipole coverage because of the lesser "leakage" [34]). Then we get the unambiguously solvable integral equation of the first type [3],

$$-\frac{1}{4\pi\beta}\int_S \sigma(q)g(p,q)dq = \phi(p), \quad p\varepsilon S \qquad (5.2)$$

for which the kernel g(p,q) of the (compressible) source potential corresponds to /18

$$g(p,q) = \{\frac{1}{\beta^2}(x_p - x_q)^2 + (y_p - y_q)^2 + (z_p - z_q)^2\}^{-\frac{1}{2}}, \quad \beta^2 = 1 - M_\infty^2 \qquad (5.3)$$

Using the relation (5.2), we can demonstrate the conjecture already stated in [10], that the three-dimensional design problem is ill-posed for this particular case, by means of a simple perturbation computation:

In order to be able to investigate conveniently the effect of small pressure fluctuations on the resulting wall shape, we approximate the control surface, Figure 6, by a circular cylinder, and limit ourselves to local rotationally symmetric perturbations in the basic u_I component. The induced supplemental potential $\delta\phi$ is then constant downstream from the perturbed site. In this region, according to Equation (5.2) it produces a likewise (nearly) constant source distribution. (Differentiation of (5.2) and then partial integration leads to the relation

$$-\frac{1}{4\pi\beta}\int_S \frac{\partial\sigma(q)}{\partial x_q}g(p,q)dq = u_I(p), \quad p\varepsilon S \qquad (5.4)$$

and accordingly σ = constant for $u_I = \emptyset$.) Its induction effect in the external field can be expressed by a line source on the center axis of the control surface running from $x = -\infty$ to $x = +\infty$. Then, from $\phi = \frac{Q}{2\pi} \ln r$ which is linear at the location of the control surface one obtains for the perturbation-induced v-component

$$v_A(\delta\phi) = \delta h'(x) \approx \frac{\delta\phi}{\bar{R} \ln \bar{R}} = \text{const.} \qquad (5.5)$$

As conjectured, a local pressure perturbation finally leads to large global contour changes, $\overline{\delta h}$.

This situation is particularly important for practically performing the external field computation because the control surface potential $\phi(p)$, because the u_I distribution is known only at the pressure holes, can be determined only up to one constant:

$$\phi(p) = \int_{-\infty}^{x_A} u_I(t, y_p, z_p)\,dt + \int_{x_A}^{x_p} u_I(t, y_p, z_p)\,dt, \quad p \varepsilon S \qquad (5.6)$$

x_A: beginning of test section

The initial potential $\phi(x_A, y_p, z_p)$ which must be determined by extrapolation can exert a considerable effect on the desired wall shape. With the C5 model, for example, there can be differences of 30% even in the interference-free case in the wall deflections at the end of the test section, depending on whether or not its flow effect is considered $(\phi(x_A, \bar{R}) = 0)$. (See Chapter 8.2.)

Furthermore, the numerical integration of the u_I distribution on the basis of the relatively small number of

support points (25 or 21 pressure holes per flexible wall, see Section 4) leads to an error (which grows in the direction of flow) in the potential determination, and therefore leads to an incorrect wall contour, especially at the end of the test section.

Direct use of the (extrapolated) u_I component as a boundary condition, on the other hand, leads to an integral equation which cannot be solved unambiguously:

$$-\frac{1}{4\pi\beta}\int_S \sigma(q)\,\frac{\partial}{\partial x_p}\,g(p,q)\,dq = u_I(p), \qquad p\in S \tag{5.7}$$

and therefore, after discretizing, to a singular equation system for the source intensity σ (see (5.4)).

Nevertheless, in order to be able to test the computed wall deflections in the simplest possible way in the present application case, the design problem is once more solved iteratively using a design method. Here the desired wall shape is determined by stepwise modification of a starting contour. The necessary geometry changes are determined from the deviation of the actual pressure distribution induced by the particular existing contour in the external field from the specified final values u_I. The design rule developed for this is derived in the next chapter.

To compute the wall pressure distributions one can select either the singularities method or the TSP method. This computation problem in the subsonic range leads to a numerically advantageous integral equation of the second type (Section 5.2.2). Even in the transsonic range it is significantly easier to solve than the comparable design problem [5,11] (Chapter 5.2.3.)

In the subsonic range the initial contour can be the straight, undeflected test section wall. In using the TSP method, though, it is better with respect to computing time to provide a good starting value using the panel program.

/21

5.2 Design Process

5.2.1 Derivation of the Design Rule

In Figure 7 we show the outer field calculation $v_A[u_I]$ carried out using the design process. In this chapter we will give a detailed description of the design rule.

The basic idea in the derivation was the observation that the pressure distribution along the (slightly) deflected test section walls corresponds approximately to that along the outer side of a geometrically similarly deformed circular cylinder. If we approximate the wall contour (averaged in the circumferential direction) by means of a sine half wave

$$h(x) = c \sin\left(\frac{\pi}{L}x\right), \quad 0 \leq x \leq L, \quad c = \text{const.} \tag{5.8}$$

then for subsonic flow $(M_\infty < 1)$ we obtain a simple analytical relationship between the flow angle change $\overline{v_D'} = h''$ and the axial perturbation speed u_D, Figure 8:

First, for the potential distribution in the outer field we have [12]

$$\phi_D(x,r) = -\frac{c}{\beta}\frac{K_0\left(\frac{\pi}{L}\beta r\right)}{K_1\left(\frac{\pi}{L}\beta \bar{R}\right)}\cos\left(\frac{\pi}{L}x\right), \quad r \geq \bar{R} \tag{5.9}$$

and from this after differentiation at the position $r = \bar{R}$ and then solving for v_D' we find

$$v_D'(x) = - \frac{\beta\pi K_1(\frac{\pi}{L}\beta\bar{R})}{L\, K_0(\frac{\pi}{L}\beta\bar{R})}\, u_D(x,\bar{R}) \qquad (5.10)$$

(5.10) corresponds already essentially to the desired design rule for the wall contour calculation, but the wavelength L has to be matched to the prevailing test conditions.

In general the measured wall pressure distribution (and also the desired wall contour) cannot be exactly defined by a single sine halfwave. Instead it will contain high frequency contributions $\omega_n = n\frac{\pi}{L}$, $n = 2,3,\ldots$ in the sense of a Fourier series expansion. In order to nevertheless be able to obtain a proportionality between v_D' and u_D, the influence of L on the proportionality factor in (5.10) was investigated in detail. The results are given for $M_\infty = 0.7$ as an example and a "basic wavelength" L = 1000 in the following table which is matched to the length of the octagon test section (half wavelength).

L	$Z = \frac{\pi}{L}\beta\bar{R}$	$\frac{K_1(Z)}{K_0(Z)}$	$-\frac{\beta\pi}{L}\frac{K_1(Z)}{K_0(Z)}$
125	1.492	1.29	- 0.023
250	0.746	1.55	- 0.014
500	0.373	2.04	- 0.009
1000	0.186	2.89	- 0.007

As can be seen, the proportionality factor increases in magnitude for the harmonics but the overall change remains relatively small. Considering the dominance of the basic wave at least for pure displacement flows and in order to provide monotonic convergence of the design cycle, we decided to use the design rule given above with a fixed value L = 1000 (see Chapter 8.2 for a discussion of convergence behavior). /23

Because of $\frac{\pi\beta\bar{R}}{L} < 0.3$ for L = 1000 the Bessel functions in (5.10) can be expressed by their symptotic expansions for a small argument [13]. The desired design rule therefore has the following final form

$$v_D'(x) = \frac{1}{\bar{R}\ \ln\left(\frac{\pi\bar{R}}{1000}\sqrt{1-M_\infty^{2}}\right)}\ u_D(x,\bar{R}),\quad M_\infty<1 \tag{5.11}$$

This corresponds essentially to the differentiated form of (5.5) and therefore not only validates this approximation formula but also the discussion there about the "ill posedness" of the design problem (5.1). The constant C_1 which occurs in the integration of v_D'

$$v_D(x) = \int v_D'(x)dx + C_1 \tag{5.12}$$

can be ignored for sufficient upstream extrapolation.

5.2.2 Post-computation process for the subsonic region (Panel method)

The calculation of the axial perturbation speed along the wall contours obtained during the individual design steps can be reduced to the following Neumann boundary value problem. /24

$$\beta^2\phi_{xx} + \phi_{yy} + \phi_{zz} = 0\ ,\quad \beta^2 = 1 - M_\infty^2 > 0$$

$$\frac{\partial\phi}{\partial n}(\vec{x}) = \delta v_D(\vec{x}),\quad \vec{x}\in S \tag{5.13}$$

$$\phi = 0\left(\frac{1}{|\vec{x}|}\right)\ ,\quad |\vec{x}| \to \infty$$

where $\vec{n}$ is the outer normal along the control surface S (Figure 6). If we produce the desired potential ϕ by a source-sink distribution

which is continuous on S (Formula 5.2, 5.3), then we obtain the source density σ as the solution of the following integral equation of the second kind

$$\frac{1}{2}\sigma(p) - \frac{1}{4\pi\beta}\int_S \sigma(q)\frac{\partial}{\partial n}g(p,q)dq = \delta v_D(p),\ p\in S \qquad (5.14)$$

The quantity $\frac{\sigma}{2}$ describes the induction effect of the source intensity $\sigma(p)dF$ located at the target point which is not contained in the integral.

As an illustration, consider a source occupation in the plane $z_q = 0$ with a target point contained in it $(x_p, y_p, 0)$. Then we have

$$g(p,q) = \{\frac{1}{\beta^2}(x_p - x_q)^2 + (y_p - y_q)^2\}^{-\frac{1}{2}}$$

and therefore

$$-\frac{1}{4\pi\beta}\int_{z_q=0} \sigma(q)\frac{\partial}{\partial z_p}g(p,q)dq = 0.$$

The integral, even though it expands over the entire plane, therefore only gives the influence (zero in this case) of the source distribution outside of the target point. The local part has to be determined separately. Application of the Gauss theorem [3], /25
on the charge element located in p, then immediately gives the relationship

$$\left(\frac{\partial\phi}{\partial n_A}(p) + \frac{\partial\phi}{\partial n_I}(p)\right)\ dF = \sigma(p)dF$$

and therefore

$$\frac{\partial\phi}{\partial n_A}(p) = \frac{1}{2}\sigma(p))$$

With this extra term, the linear equation system which approximates (5.14) takes on a very favorable numerical property (see below).

In order to perform the discretization, the control surface is divided up into flat quadratic surface elements Δ_j, the so-called panels

$$S = \bigcup_{j=1}^{N} \Delta_j \tag{5.15}$$

and the desired singularity intensity is approximated by a step function (panel method of first order)

$$\tilde{\sigma}(q) = \sigma_j = \text{const.}, \quad q \in \Delta_j, \quad j = 1, \ldots, N \tag{5.16}$$

For the normal speed $\tilde{v}$ induced in $p \in S$ we then find

$$\tilde{v}(p; \sigma_1, \ldots, \sigma_N) = \frac{1}{2}\tilde{\sigma}(p) - \frac{1}{4\pi\beta}\sum_{j=1}^{N} \sigma_j \int_{\Delta_j} \frac{\partial}{\partial n} g(p,q)dq \tag{5.17}$$

/26

The constants $\sigma_1, \ldots, \sigma_N$ have to be matched so that the boundary conditions δv_D are approximated as well as possible. This is done most simply by the so-called "point-matching", [3], in which the approximation function is determined in such a way that it exactly agrees with the prescribed distribution at fixed points of the definition region. In the present case one selects a "control point" p_i on each panel and then from the requirement

$$\tilde{v}(p_i; \sigma_1, \ldots, \sigma_N) = \delta v_D(p_i), \quad i = 1, \ldots, N \tag{5.18}$$

one finds the linear equation system

$$\sum_{j=1}^{N} A_{ij}\,\sigma_j = \delta v_{D,i}, \qquad i = 1, \ldots, N \tag{5.19}$$

with the influence coefficient

$$A_{ij} = \begin{cases} \frac{1}{2} & i = j \\ -\frac{1}{4\pi\beta} \int_{\Delta_j} \frac{\partial}{\partial n} g(p_i,q)dq & i \neq j \end{cases} \tag{5.20}$$

The calculation of A_{ij} is performed in the Appendix (Section 13). In addition to the exact formulas, we give simple approximations in the form of a multipole expansion, which can be used for a large distance between the target point and the induced panel, [17].

/27

The diagonal elements $A_{ii} = \frac{1}{2}$ are much larger compared with the other coefficients and are very advantageous for the numerical solution of (5.19). Therefore iteration methods can be used for this. This is important for practical applications, because due to the memory requirements of direct methods (Gauss-Elimination, etc), there can be restrictions on the number of surface segments. (The coefficient matrices which occur during the discretisation of the integral equations of the first kind, see for example (5.2), have as a rule no dominating diagonal and can only be solved directly).

However, we should not forget the fact, that the values $\sigma_1, \ldots, \sigma_N$ calculated from (5.19) only represent a usable approximation for the desired force intensity σ (Equation (5.14) if the panel coverage of the control surface is appropriate). This discretisation error

$$\delta Q = \int_S |\sigma(q) - \tilde{\sigma}(q)| \, dq \tag{5.21}$$

can be simply reduced by increasing the number of elements. But especially in the present application, restrictions can be brought about by the limited performance of the wind tunnel computer. However, the deflections of the test section walls only have to be determined within the adjustment accuracy of the past transducers (maximum) (it is 0.03 mm in the model area and 0.07 mm for the octagon test section). (The influence of the wall contour accuracies on the model flow is discussed in Section nine).

In order to find a panel coverage which is efficient for this, we first determine the adapter wall shape for two typical flow cases (C5 and F4 model represented by singularities).

This was done with a very fine segmentation of the control surface (16 x 30 elements) using a large computer. After this the number of panels was reduced with consideration of the local source gradient according to the tolerance specified above. The optimized paneling is given in Figure 9. It consists of 16 strips (according to the 8 flexible walls with intermediate lamella pieces (Figure 6), which are 15 elements each of different lengths. The detailed discretisation in the circumferential direction is required because of the necessity for covering the vortex train which induces lift along the rear test section region. However, since only symmetric models without slip angles are investigated, the resulting linear equation system (5.19 can be reduced to only 9 x 15 - 135 nonredundant individual equations.

/28

The numerical solution of the boundary value problem (5.13) is

$$\tilde{\phi}(p) = -\frac{1}{4\pi\beta} \int_S \tilde{\sigma}(q) g(p,q)\,dq \,, \quad p \in S \cup B_e \tag{5.22}$$

where $\tilde{\sigma}$ is the calculated approximation according to (5.16) and (5.19). The desired perturbation speed $\delta\tilde{u}_e$ along the control surface is then obtained by differentiation

$$\delta\tilde{u}_E(p) = \frac{\partial\tilde{\phi}}{\partial x_p}(p) = -\frac{1}{4\pi\beta} \int_S \tilde{\sigma}(q) \frac{\partial}{\partial x_p} g(p,q)\,dq, \quad p \in S \tag{5.23}$$

An evaluation along the control points p_i, $i = 1, \ldots, N$ gives

$$\delta u_{E,i} = \sum_{j=1}^{N} B_{ij}\sigma_j \tag{5.24}$$

/29

with the influence coefficient

$$B_{ij} = -\frac{1}{4\pi\beta} \int_{\Delta_j} \frac{\partial}{\partial x_p} g(p_i,q)\,dq \tag{5.25}$$

and the calculation is also given in the Appendix.

A combination of (5.19) and (5.24) then leads to the very simple linear relationship

$$\delta\vec{u}_E = BA^{-1}\delta\vec{v}_D \tag{5.26}$$

where the matrix BA^{-1} formed from the influence coefficients can be determined before the test. The post calculation task in the subsonic case therefore can be reduced to the use of a panel method and a simple matrix vector multiplication.

5.2.3 Post-computation process for the subsonic region (TSP method)

In order to also discuss the case of incident flow near the speed of sound, the post calculation part of the design cycle can also be done using a TSP method. The corresponding computer program was made available by AEDC [5] and will be briefly discussed.

We solved the classical Guderley-von Karman equation [10] in the conservative formulation

$$\left[(1-M_\infty^2)\phi_x - \frac{\kappa+1}{2} M_\infty^2 \phi_x^2\right]_x + \frac{1}{r}\left[r\phi_r\right]_r + \frac{1}{r}\left[\frac{1}{r}\phi_\theta\right]_\theta = 0$$

with the boundary condition /30

$$\frac{\partial\phi}{\partial r}(x, \bar{R}, \theta) = \delta v_D(x,\theta)$$

and the circular cylindrical assumed control surface (Radius $\bar{R}$) and

$$\phi \to 0 \quad r \to \infty$$

$$\phi_x \to 0 \quad |x| \to \infty \tag{5.27}$$

in the far field.

Based on the symmetry relationships $(\phi(x,r,\theta) = \phi(x,r,-\theta))$ we finally find

$$\phi_\theta(x,r,0) = \phi_\theta(x,r,\pi) = 0 \quad , \quad r \geq \bar{R}$$

The difference network was matched to the present application case and now extends in the range

$$|0 \leq x \leq 940| \times |83 < r < 332| \times |0 \leq \theta \leq \pi| \text{ with } 31 \times 10 \times 11 = 3410$$

points. The discretisation of the space derivatives and the solution of the resulting difference equations is done using standard technique (finite difference method of Murman, SLOR-relaxation method) which are discussed in detail in [10] and [18].

The numerical complexity for calculating the desired perturbation speed distribution $\delta u_E(S) = \frac{\partial \phi}{\partial x}(S)$ is of course much more than for the subsonic case. Therefore, considering the desired Online wall adaptation, one should use the simple relationship (5.26) as much as possible.

The range of the validity of the linear potential equation is discussed in detail in Section 9.

6. OPTIMIZATION OF THE RATE OF CONVERGENCE FOR THE WALL ADAPTATION PROCESS /31

6.1 Subsonic Case

6.1.1. Convergence Behavior for Constant Regulation Factor

By a suitable selection of the regulation factor K we wish to increase the convergence rate of iteration wall adaptation method (3.3) similar to the two-dimensional case.

A first indication about the effect of K on the adaptation method was found from demonstration tests in the octagon test section of the TU Berlin. It was found that an adaptation of the test section walls was only possible with very small regulation factors ($K \leq 0.10$) and relatively numerous (≥ 10) iteration steps. For larger values of K one found oscillating wall contours with rapidly increasing deflections, which already lie outside of the permissible displacement paths of the past transducers after a few iteration steps.

In order to make a systematic investigation of this experimental finding, we performed a numerical simulation of the regulation algorithm (Figure 2). The wall pressure distribution $u_I^{(n+1)}$ is not determined by means of the wind tunnel tests in the individual adaptation steps, but instead using a natural assumption about the given wall contour $v_I^{(n+1)}$.

Let us start the simulation with the measured values $u_I^{(1)}$, $v_I^{(1)}$ and define

$$u_I^{(2)} = u_I^{(1)} + \delta u_I^{(2)}$$

$$\delta v_I^{(2)} = v_I^{(2)} - v_I^{(1)} \qquad (6.1) \qquad /32$$

Then one can establish between $\delta u_I^{(2)}$ and $\delta v_I^{(2)}$ (accordingly for $\delta u_I^{(n+1)}$ and $\delta v_I^{(n+1)}$ in the following iterations) an analytical relationship corresponding to (5.26), if we assume that the flow field induced by contour change $\delta v_I^{(2)}$ is irrotational and the potential $\delta\phi^{(2)}$ satisfies differential equation (5.1a). These conditions are satisfied because of the assumed small wall deflections, to a great degree of accuracy [7,9].

The trial solution (the loop index is omitted)

$$\delta\phi(p) = -\frac{1}{4\pi\beta}\int_S \zeta(q)g(p,q)dq \;, \quad p\varepsilon B_i US \qquad (6.2)$$

then leadsto the following integral equation of the second kind for ζ

$$\frac{1}{2}\,\zeta(p) - \frac{1}{4\pi\beta}\int_S \zeta(q)\,\frac{\partial}{\partial n_I}\,g(p,q)dq = -\,\delta v_I(p), \quad p\varepsilon S \qquad (6.3)$$

when we finally find the desired increment δu_I as

$$\delta u_I(p) = -\,\frac{1}{4\pi\beta}\int_S \zeta(q)\,\frac{\partial}{\partial x_p}\,g(p,q)dq, \quad p\varepsilon S \qquad (6.4)$$

After performing the discretisation discussed in Chapter (5.2.2) we then find the two linear relationships

$$\begin{aligned} A'\vec{\zeta} &= -\,\delta\vec{v}_I \\ \delta\vec{u}_I &= B\vec{\zeta} \end{aligned} \qquad (6.5)$$

and the influence coefficients F'_{ij} can be expressed by the already defined A_{ij} (5.20) /33

$$A'_{ij} = \begin{cases} A_{ij} & i = j \\ -A_{ij} & i \neq j \end{cases} \qquad (6.6)$$

A comparison of (6.5) with the corresponding relationships (5.19) and (5.24) for the outer flow

$$\begin{aligned} A\vec{\sigma} &= \delta\vec{v}_A \\ \delta\vec{u}_A &= B\vec{\sigma} \end{aligned} \qquad (6.7)$$

immediately shows that the same wall contour change $(\delta\vec{v}_A = +\,\delta\vec{v}_I)$ in the outer field produces a much lower pressure fluctuation than inside the test section. This then makes understandable the adaptation behavior discussed above.

This state of affairs is found from the estimation

$$A_{ij} > 0 \quad , \quad i,j = 1, \ldots, N \qquad (6.8)$$

which follows immediately from the convex nature of the volume inside the control surface, Figure 9. In the outer field calculation (6.7) the singularities therefore mutually support one another with their induction effect. This means that for producing a prescribed deflection $\delta\vec{v}_A$, a smaller charge density σ is required. However, for the inner flow we find

$$\sum_{j=1}^{N} A'_{ij} \approx 0 \quad , \qquad i = 1, \ldots, N \tag{6.9}$$

Equation (6.3) for $\delta v_I(p) = 0$ has a nontrivial solution /34
ζ=const because a constant source distribution produces a constant potential along the control surface and therefore inside of it as well. See (5.4)). In this case the induced normal speeds approximately cancel and one requires a large source-sink intensity in order to obtain the same contour change $+\delta v_I$. Since δu_I and δu_A are determined from the same matrix B, we obtain the assumed physical state of affairs.

The results of the simulation are given in Figure 10 for a typical flow case [19]. (In the Appendix we also give an analytical investigation of the convergent behavior). As expected, the adaptation method only converges for very small regulation factors $K \leqslant 0.06$. One remarkable feature is the large increase in the number of iterations for factors larger than the optimum value $K_{opt} \approx 0.056$ and the ensuing transition to divergence. Report [9] gives an account of a similar result during the adaptation of three-dimensional flows around wings. The numerical simulation therefore not only confirms the experimental results but also shows that even if one uses an optimum regulation factor, the matching of the test section walls requires an excessive number of intermediate steps and therefore long wind tunnel testing times.

In the next section we will show that by means of a differentiated weighting of the channel line flow and the outer flow, one can achieve a drastic increase in the convergence rate.

6.1.2 Single-Step Method /35

We again start with the measured values $u_I(S)$, $v_I(S)$ and the outerfield calculation $v_A[u_I]$. We then investigate how one can obtain the best possible approximation for the desired adapted wall shape.

For the mathematical description of the problem we will formally decompose u_I and v_I into the model part without interference and the influence of the wall.

$$u_I = u_\infty + u_W$$
$$v_I = v_\infty + v_W \qquad (6.10)$$

Based on the linearity of the outer flow we then find

$$v_A[u_I] - v_I = v_\infty + v_A[u_W] - v_\infty - v_W = v_A[u_W] - v_W \qquad (6.11)$$

The design task $v_A[u_W]$ can then be solved in two steps according to (6.7). In this case the singularity intensity σ is of course unknown. On the other hand, the wall-induced perturbation speed field satisfies the linear potential equation (5.1.a), to a good approximation, so that we can also use the relationships (6.5) discussed in Section 6.1.1.

Overall, we obtain the following four equations

$$A\sigma = v_A[u_W] \qquad A'\zeta = -v_W \qquad (6.12)$$
$$B\sigma = u_W \qquad B\zeta = u_W$$

and from this because of (5.4), (6.9), (6.6), (5.20) /36

$$\zeta = \sigma + c \,, \qquad c = \text{const.} \tag{6.13}$$

$$v_A[u_W] - v_W = A\sigma + A'(\sigma+c) = (A + A')\sigma = E\sigma = \sigma \tag{6.14}$$

where E is the unit matrix.

Together with (6.11) we then obtain the following formula for the wall dependent perturbation potential

$$\phi_W(p) = -\frac{1}{4\pi\beta} \int_S \{v_A(q) - v_I(q)\} \; g(p,q) \; dq \tag{6.15}$$

(for $v_A[u_I]$ we will write v_A in the following.as an abbreviation).

The (known) difference $v_A(S) - v_I(S)$ therefore is not only a "measure" for the wall interference (see (3.2)), but also determines it uniquely. It should be noted that this statement does not require any additional assumptions about the model-induced perturbation field.

Application of (6.14) directly leads to the

Single step form

$$v_\infty = v_I - v_W = v_I + A'(v_A - v_I) = v_I + (E-A)\,(v_A - v_I) \tag{6.16}$$

The adapted wall contour can therefore be determined already from the measured values of a single wind tunnel test (within the range of validity of the linear potential equation). /37

This can be done even without numerical additional complexity because the matrix A already has to be calculated once (Chapter 5.2.2). As a comparison which (3.3) shows, the enormous gain in convergence is based on the replacement of the constant regulation factor by the "regulation matrix" E - A which considers the incident Mach number and the control surface geometry.

In this connection we should emphasize that already before a single step method for three-dimensional wall adaptation was developed at the DFVLR and was used successfully [7]. The Fourier trial solution selected there for representing the wall-induced perturbation potential however, has substantial practical disadvantages compared with the singularity method, such as for example a complicated formalism and the fact that one cannot transfer to other control surface cross sections. A comparison of the two methods using measured values from the "expandable adaptive test sections" of the DFVLR is performed in Section 8.3. After this, we report about experimental results in the octagon test section.

Since relationship (6.15) can be used without model representation, it is very useful even alone. One can therefore develop a high performance correction method. In addition, it is the foundation of the new method for testing 3D bodies in wind tunnels with two flexible walls, discussed in Chapter 10.

6.2 Transsonic Case

The regulation matrix E - A defined in the previous section depends continuously on the intimate Mach number and for $M_\infty \to 1$ goes to a well defined limit value (formerly discussed in Appendix). Since the TSP method (Chapter 5.2.3) only can be used for flow near the speed of sound, considering (6.16) the following algorithm of wall adaptation promises a fast conversion. /38

$$v_I^{(n+1)} = v_I^{(n)} + (E-A)\Big|_{M_\infty=1} \left(v_A[u_I^{(n)}] - v_I^{(n)}\right), \qquad (6.17)$$

$$n = 1, 2, \ldots$$

In contrast to the subsonic case, more iteration steps will be necessary in general.

7. EXTRAPOLATION AND CORRECTION OF THE MEASURED PRESSURE DISTRIBUTION

In order to transfer the Cp distribution determined along the wall pressure traps to the panel control points, Figure 9, the measured values have to be interpolated in two dimensions and have to be extrapolated beyond the test section region. By a continuation upstream at the same time, we wish to specify the effective incident speed U_{eff} and if necessary a correction to the boundary conditions u_I have to be performed.

In the derivation of the extrapolation method developed for the octagon test section, we started with the usual singularity representation of the model and the flow [21]:

Point Dipole for Simulation of Model Displacement

Horseshoe Vortex for Representing the Model Lift

Point Source for Representing the Wake (Including Model Spear)

Because of the different induction behavior of these singularities, it is immediately found that the perturbation pressure distribution which prevailed at both test section ends can be attributed mainly to the influence of the wake. In the extrapolation of the wall measured values, we only have to consider the source effect. (The vortices in the wake are assumed to align parallel to the incident flow. Transverse flow components are ignored). This procedure not only gives physically reasonable results, but also avoids the numerical difficulties associated with a detailed flow simulation [22].

The calculation of the wake source has no problems because due to the impermeable channel walls, it is given independent of their deflection, by the fictitious mass flux difference between the test section beginning ($x=x_A$) and the final cross section ($x=x_E$).

If we call the axial total speed distribution measured at the pressure caps d_{ij}, $i = 1,\ldots,8$, , $j=1,\ldots,26$ $U_{ges}(d_{ij})$, then by introducing the nominal (uncorrected) incident speeds (Mach number M_∞) we find

$$U_\infty = U_{ges}(d_{i1}) \qquad (7.1)$$

for the (model and wall-induced) perturbation part

$$u_I'(d_{ij}) = U_{ges}(d_{ij}) - U_\infty \qquad (7.2)$$

By using the Gauss theorem we find [3] the following for the desired force intensity

$$q = \int_{F_E} u_I'(x_E,y,z)df - \int_{F_A} u_I'(x_A,y,z)df$$

$$\approx \frac{1}{8} \sum_{i=1}^{8} u_I'(d_{i,26}) \cdot F_E = \bar{u}_I'(x_{D,26}) \cdot F_E \qquad (7.3)$$

and this can be calculated without any problems during test operations.

The induction effect of this source of course depends on the contour of the test section walls and therefore we will separately investigate the two cases of strong and weak wall influence:

(aerodynamically) straight walls: /41

The source produces a constant perturbation speed which is the same (in magnitude) over the cross section at the two test section ends due to symmetry, δu. Together with (7.3) we find

$$\delta u(x_E) = - \delta u(x_A) = \frac{1}{2} \bar{u}_I'(x_{D,26}) \qquad (7.4)$$

In this wall configuration, consequently we find a non-vanishing full effect of the model in the flow, which has to be considered by a corresponding correction of the incident flow conditions. Because of (7.1) and (7.4) the corrected (effective) incident speed U_{eff} is then calculated as

$$U_{eff} = U_\infty - \delta u(x_A) = U_\infty + \frac{1}{2}\,\bar{u}_I'(x_{D,26}) \qquad (7.5)$$

which brings about a change in the incident flow Mach number of

$$\Delta M_\infty = \left(1 + \frac{\kappa-1}{2}\,M_\infty^2\right) M_\infty \cdot \frac{1}{2}\,\bar{u}_I'(x_{D,26}) \qquad (7.6)$$

[21].

From (7.5) and (7.2) we finally obtain the corrected axial perturbation speed

$$u_I(d_{ij}) = U_{ges}(d_{ij}) - U_{eff} = u_I'(d_{ij}) - \frac{1}{2}\,\bar{u}_I'(x_{D,26}) \qquad (7.7)$$

/42

which according to (7.4) can be continued beyond the test section region using

$$u_I(x) = \begin{cases} -\frac{1}{2}\,\bar{u}_I'(x_{D,26}) , & x < x_{D,1} \\ \\ \frac{1}{2}\,\bar{u}_I'(x_{D,26}) , & x > x_{D,26} \end{cases} \qquad (7.8)$$

The transfer of this extrapolated u_I distribution to the panel control points is then done using a two-dimensional cubic spline [23].

Deflected walls:

Based on the single step formerly discussed in Section 6.1.2, we will restrict ourselves to the case of almost adapted test section walls.

We obtain the following for the perturbation speed induced upstream by the weight source

$$\delta u(x_A) \sim \frac{q}{(x_A - x_{NL})^2} \tag{7.9}$$

where (x_{NL} = 600, 0, 0) is the position of the singularity in the tunnel.

A connection of the incident flow conditions therefore is in general not necessary if there is only a weak wall influence. Almost the entire source induced mass flux (7.3) therefore passes the rear test section cross section, so that the following extrapolation of the perturbation speed distribution (7.2) makes physical sense. /43

$$u_I'(x) = \begin{cases} 0 & x < x_{D,1} \\ \bar{u}_I'(x_{D,26}) & x > x_{D,26} \end{cases} \tag{7.10}$$

The interpolation of the boundary conditions to the panel control points is again done using the already mentioned 2D-spline method.

8. TESTING OF THE ADAPTATION SOFTWARE

8.1 Structure of the Program Systems

Figure 11 shows the programming system for the three-dimensional wall adaptation in the subsonic case. It consists of three separate main programs, which are coupled with data transfer.

The geometry program "GEO" defines the panelling of the control surface using the reading surface points (Figure 9). The calculated coordinates of the panel corners are transferred together with the selected incident Mach number M_∞ using the program "EINFL" for determining the influence coefficients A_{ij}, B_{ij} (Chapter 5.2.2). The storage of the calculated values is done in the form of the two matrices BA^{-1} and A considering their further use in the Program "ADAP1". The structure of ADAP1 is given in Figure 12. The three important features are:

(1) Extrapolation and correction of the measured pressure distribution (Chapter 7)
Transfer of u_I and v_I to the panel control points

(2) Outerfield calculation $v_A[u_I]$ using the design method (Chapter 5.2).

(3) The evaluation of the single step formula (Chapter 6.1.2).

With the calculation of the two influence matrices the program Parts (2) and (3) are reduced to a simple matrix vector multiplication, so that a fast calculation of the adapted wall contour is assured (see Chapter 9).

/45

For the adaptation in the transonnic case, a separate computer program "ADAP2" was written. Its structure is similar to that of "ADAP1", but within the framework of the outerfield calculation we used the difference method developed by AEDC for the transsonic case (Chapter5.2.3). The regulation matrix $(E - A)\big|_{M_\infty} = 1$ (Chapter 6.2) is determined in another sub-program (as can be seen from the formulas in the Appendix, this can be reduced to the size 5 x 5 for $M_\infty = 1$).

However, in this case, the wall contour calculation requires a large amount of calculation time and memory and therefore cannot be done on line (Chapter 9).

8.2 Analytical Test Case

Ths computer programs for wall adaptation are tested using analytical test cases and by close calculation of known experimental results. The calculations used for control of the TSP method are discussed in detail in [29]. In this section we will discuss the theoretical test runs with "ADAP1".

The simulation of an interference flow field in the octagon test section was performed using singularities. As a model we used the rotationally symmetric ONERA C5 body, Figure 16a, which has displacement effects which can be represented in a known way by sources and sinks along its axis of rotation [14]. We then find the following closed solution for the model induced potential.

/46

$$\phi(x,r) = -\frac{1}{4\pi}\int_0^{\ell} \frac{F'(\xi)}{|(x-\xi)^2+\beta^2 r^2|^{\frac{1}{2}}}\, d\xi \quad , \beta^2 = 1-M_\infty^2 \qquad (8.1)$$

where $F'(\xi)$ is the cross section area change and ℓ is the length of the body. If we introduce

$$F'(\xi) = \frac{1}{2}\pi d(\xi) d'(\xi) \qquad (8.2)$$

the model thickness distribution $d(\xi)$ as a geometric quantity in (8.1), then we find from it after partial integration the easy to evaluate formula

$$\phi(x,r) = \frac{1}{16}\int_0^{\ell} \frac{d^2(\xi)\,(x-\xi)}{[(x-\xi)^2+\beta^2 r^2]^{\frac{3}{2}}}\, d\xi$$

$$-\frac{1}{16}\frac{d^2(\ell)}{[(x-\ell)^2+\beta^2\, r^2]^{\frac{1}{2}}} \qquad (8.3)$$

The term outside of the integral occurs because the rear model diameter (d(ℓ) was not made zero in order to simulate that model sphere.

From the two velocity components obtained by differentiation of (8.3) we can calculate as usual the static pressure and the interference -free streamline course everywhere in the flow. /47

In order to represent the influence of the wall, we used the panel method discussed in Chapter 5.2.2. The singularity intensity along the panels was determined in such a way using Equation (6.3) so that after superposition with the model induced flow field (8.3), the kinematic boundary condition

$$v_I = -\frac{\partial \phi}{\partial r} + \frac{\partial \phi_W}{\partial n_I} = 0 \qquad (8.4)$$

is exactly satisfied along the control surface (C5-body in the octagon test section with non-deflected walls).

The resulting u-distribution at the points of the wall pressure shafts

$$u_I = \frac{\partial \phi}{\partial x} + \frac{\partial \phi_W}{\partial x} \qquad (8.5)$$

together with the incident flow Mach number M_∞ and the values $v_I = 0$ (Equation 8.4) were then the input data for the adaptation program "ADAP1". The adapted wall shape calculated with (single step) method in addition to the corresponding pressure distribution was then compared with the exact interference free variables calculated from (8.3) as a check.

Figure 13 gives results for a test section wall at $M_\infty = 0.7$. The agreement of the calculated wall pressure distributions is satisfactory overall, even though the extreme values were not exactly achieved. The variation of the wall deflections calculated

using "ADAP1" agree also quite well with the corresponding adapted contour. The somewhat larger deviations at the end of the test section are still acceptable considering the past transducer tolerance of 0.07 mm there. Also, one can achieve an improved reproduction by an exact determination of the u_I-distribution input to "ADAP1" (8.5) (more panels for representing the influence of the wall). /48

Figure 14 shows the typical convergence behavior of the design method represented using values for the analytical flow case discussed above ($M_\infty = 0.7$). The accuracy ε is defined by the mean relative deviation between the actual and nominal distribution at the individual designed steps (see Figure 7)

$$\varepsilon = \frac{1}{N} \sum_{k=1}^{N} \frac{|u_I(k) - u_E(k)|}{\max\limits_{1 \leq k \leq N} |u_I(k)|} \qquad (8.6)$$

(N = number of control points).

One can see the continuous improvement of the designed wall contours. The convergence range decreases continuously during the iteration. This phenomenon is to be attributed to the existence of harmonics in the approximating u_I distribution. As already discussed in Chapter 5.2.1, these contributions can be found by iteration using an adapted design rule. However, in practice it has been found that already after three to four iteration steps, the designed wall shape is sufficient for calculating an adaptive contour (see Chapter 8.3 and 9). Therefore, no modification to the design rule (5.11) was necessary.

8.3 Result Comparison with DFVLR Adaptation Program

As already mentioned in 6.1.2, the DFVLR has their own single step method based on the Fourier method for regulation of its three-dimensional adaptive test section (DAM). It has been used successfully. The wall contours calculated with this program are therefore "experimentally verified" and can be used to test the present adaptation algorithm.

The two flow cases post calculated with ADAP1 from the "DAM" are shown in Figures 15a and 15b together with the DFVLR reference values [7, 31]. We show the results for the first adaptation step, that is, the wall deflections and pressures calculated based on wall pressure distributions measured for aerodynamically straight walls.

Figure 15a shows the comparison for the FFA model (parabolic spindle) for 0° angle of attack and the nominal incident Mach numbers $M_\infty = 0.5$. Since this is a flow with rotational symmetry, we only show the wall contour and the pressure distribution averaged in the circumferential direction. As can be seen, the runs calculated with ADAP1 agree well with the corresponding reference data. The remaining small deviations can be attributed to the additional physical correction of the input pressure measured values in the TUB method (see Chapter 7). The effective incident flow Mach number in this case is found to be $M_{kor} = 0.5036$ (blockage 3.1%), a value /50 where the upstream of the model has been removed.

Figure 15b shows corresponding comparison calculations for a wing-fuselage combination. This is the AGARD calibration model B with 4° incidence angle and $M_\infty = 0.5$. The reference values again are well reproduced. The Mach number correction is now $\Delta M_\infty = 0.006$ for a blockage ratio of 3.5%.

The good agreement of the calculated results in both flow cases therefore clearly verifies the numerical methods of wall adaptation developed here, (design algorithm, single step formula).

/51

9. EXPERIMENTAL RESULTS

9.1 Tested Models

Three models were made for testing the 3-D adaptive test section.

A rotationally symmetric body, the ONERA C5 calibration model, is used for pressure measurement. It has 21 static pressure caps distributed over the entire model length of 166.27 mm, Figure 16a. Its maximum diameter of 24 mm leads to a blockage ratio of 2% in the octagon test section. With this model, the first successful 3D wall adaptation was achieved at the TUB.[30].

The ZKP-F4 model, Figure 16b, has an Airbus-like cross section with a transsonic wing (Span 120 mm). It is designed for force measurements which are performed with a three component balance installed in the fuselage. Its blockage in the 3D test section is 1.2%.

Figure 16c shows the Canard configuration used for pressure and force measurements. The Delta shaped wing has an area which is about 4 times larger than the F4 wing with the same span of 120 mm (aspect ratio, 2.29). In this way one obtains not only much larger normal forces, but also remarkable risk differences between measurements for straight and adapted channel walls. Also large changes in the moment variation produced by the effect of the Canard control surface, so that the model is especially well suited as an indicator for wall interferences. /52

The static pressure can be measured from 10 pressure caps distributed over the fuselage. The blockage of the model is 1.3% in the octagon test section.

9.2 Calibration of the 3D Test Section

Before installing the model, the test section has to be calibrated, that is,the perturbation of the parallel basic flow due to the wall boundary layer has to be compensated for by a preliminary deflection of the flexible walls. In the case of the octagon section, an additional expansion was necessary in order to equalize the displacement effect of the model sphere.

The resulting (aerodynamically straight) wall contour is shown in Figure 17 for an incident Mach number of $M_\infty = 0.8$. Here we are dealing with a photographic picture of the color monitor, which is used for the graphic recording of adjusted wall shapes during the tests. The deflections are given in mm (wall 1-4 top, wall 5-8 lower part of the image). The values are interpolated linearly at the actuators over the test section length.

By means of the same preliminary adjustment shown in the circumferential direction, (the deviation in the sphere region is produced by the missing ninth actuator term along the top and lower wall) we obtain an almost constant pressure distribution at least in the region of the model. Large differences occur at the test section beginning before the first actuator because of residual wall boundary layer influences. They also occur at /53
the rear part by the not exactly compensated for displacement influence of the sphere.

In order to assure a reliable wall adaptation later on, we decided to only use the wall pressures measured between the first and eighth actuator for calculating the external field. The other measured values are in place by an extrapolation according to Equation 7.10:

$$u_I'(x) = \begin{cases} 0 & x < x_{D,4} \\ \bar{u}_I'(x_{D,20}) & x > x_{D,20} \end{cases} \qquad (9.1)$$

The also described correction of the pressure distribution for aerodynamically straight test section walls discussed in Section 7 did not seem to make sense considering the poor pressure measured values at the two test section ends discussed above.

9.3 Measurement Results with the Canard Model

In this chapter we will use the example of selected results for the Canard model to demonstrate the high performance capability of the adaptive octagon test section. An extensive documentation of test results is obtained in [32].

For the test execution, one important feature was the definition of a practical truncation criterion for wall adaptation. One possible indicator for this is the convergence behavior of values measured on the model (forces, pressures) or axis · the change in the adjusted wall shape in following regulation steps. Of course, eventually /54 constant wall contour also then leads to constant model measured values. However, in the last analysis, removal of the interferences is only required in the region of the configuration in the flow. Since the wall-induced perturbations towards the mode decreased ($M_\infty < 1$), this has a direct influence on the accuracy limit with which the adapted wall shape has to be determined (see Equation 3.4)). This effect is discussed in the next section for the special case of a rotationally symmetric flow. The estimation obtained there is too "sharp" in practice, because a possible extinction of wall interferences in the model region is not considered. As a basis for evaluating the adjusted wall deflection, we therefore use the behavior of the model measured values.

The typical sequence of wall adaptation is illustrated in the following table.

	Flat walls	1. WK	2. WK	3. WK
C_A	.207	.159	.172	.168
C_W	.030	.025	.027	.025
C_{M25}	.031	.035	.034	.034

Canard-Model
$M_\infty = 0.7, \alpha = 4.54^o$

This shows the change in the forces measured on the Canard Model at the individual adaptation steps for the incident flow conditions $M_\infty = 0.7$, $\alpha = 4.54°$. The difference in the coefficients from the second to the third wall contour already is within the range of the reading accuracy of the balance reading, so that the test section walls can be considered to be adapted.

As a check, we compared the measured wall pressure distribution /55 after the last regulation step with those calculated for the outer field. As discussed in Chapter 3, they have to agree for the adapted wall contour. For the flow case under consideration, a comparison like this is given in Figure 18 for the upper flexible wall. For clarity of the wall interferences, we also show the pressure distribution measured for aerodynamically straight walls. It can be seen, that the third wall contour canalso be considered to be almost adapted even in the "strict" sense. The remaining pressure differences in the front area of the model suspension apparently are truncation effects, which are caused by the effective shortening of the test section along the section between the first and eighth actuator (see Chapter 9.2). For the two rear actuators 9 and 10, we also did not calculate any deflections, but instead retained the constant preliminary adjustment used for the prevailing incident Mach number.

As an example for the wall deformations to be adjusted, Figure 19 shows the adapted contour for the Canard model at $M_\infty = 0.8$ and $\alpha = 8.04°$. The dominating influence of the downwind field is especially remarkable, which requires a relatively large dropping of the rear test section cross section (eighth actuator).

The necessary moving back of the wall shape in the forward region does not have any important effects on the data measured on the model, as the corresponding wind tunnel tests show.

The next experimental proof of the high quality of the wall adaptation is shown in Figure 20. It shows the pitch moment polar measured at $M_\infty = 0.7$ for the Canard model for straight and adapted test section roles. For comparison, we show also the measured polars in the adaptive profile T2 of the ONERA and the polars obtained at the "DAM" for the model. /56

These measured values can be considered to be free of interference because of the very small blockage ratios (DAM 0.06 %, T2 0.18%). The T2 tunnel was adapted according to the method developed by Wedemeyer (see Chapter 10). The very accurate reproduction of the interference - free moment variation in the octagon test section is especially remarkable, because the polar indicates strong wall interferences for straight walls. A corresponding comparison for the $C_A(\alpha)$ and $C_A(C_W)$ polar is given in [32].

In order to determine the adaptive wall shape, the panel method was used for all tests performed - (Program "ADAP1"). The average calculation time per adaptation step was 45 seconds in the wind tunnel computer HP 1000F. In order to adjust the test section walls, in general 1-2 intermediate steps were required. The adaptation was always started with aerodynamically straight walls in order to demonstrate the wall interference. It was only at the incident Mach number $M_\infty = 0.95$ that oscillating wall contours occurred at higher incidence angles of the Canard model, so that a reliable adaptation could not be reached. This unfavorable regulation behavior was certainly attributable to the very poor flow quality in the test section for flow near the speed of sound (turbulent separation in the nozzle).

/57

On the other hand, the measured wall pressure distribution showed local supersonic zones for aerodynamically straight walls. This means that the contour determined with the panel method could have been wrong. An additional calculation with the TSP adaptation program indeed showed somewhat different deflections as is shown in Figure 21 for the upper and lower test section wall.

After improving the flow quality in the test section we wish to examine with experiments to what extent these differences affect the model flow.

9.4 Influence of the Wall Contour Inaccuracies on the Floor on the Model

In this chapter we will estimate how accurately the test section walls have to be adjusted in order to reduce remaining interferences in the model measured values through a specified amount. For clarity, we will investigate only the effects of perturbations in the adapted wall contour which has rotational symmetry

$$\delta h\,(x,\bar{R}) = \Sigma\; A_n \sin(\omega_n x),\ \omega_n = n\,\frac{\pi}{L},\ n = 1,2,\ldots \qquad (9.2)$$

The perturbation flow induced inside the test section then satisfies the two-dimensional potential equation

$$\beta^2\phi_{xx} + \frac{1}{r}\,\phi_r + \phi_{rr} = 0\ ,\quad \beta^2 = 1 - M_\infty{}^2 > 0 \qquad (9.3)$$

with the boundary condition

$$\phi_r\,(x,\bar{R}) = \delta h'(x) = \Sigma\; A_n\omega_n \cos(\omega_n x) \qquad (9.4)$$

The solution is (see Chapter 5.2.1)

$$\phi(x,r) = \frac{1}{\beta}\;\Sigma\, A_n\cos(\omega_n x)\,\frac{I_o(\omega_n\beta r)}{I_1(\omega_n\beta\bar{R})}\ ,\quad r \leq \bar{R} \qquad (9.5)$$

For the perturbation speed along the tunnel axis $r = 0$ and therefore in the region of the model in the flow we have

$$u(x,o) = \phi_x(x,o) = -\frac{1}{\beta} \sum \frac{A_n \omega_n}{I_1(\omega_n \beta \bar{R})} \sin(\omega_n x) \quad (9.6)$$

The comparison (9.6) and (9.2) shows that the wall contour perturbations decay towards the center of the tunnel, and the damping factor is given by

$$D(\omega_n) = \frac{\omega_n}{\beta I_1(\omega_n \beta \bar{R})} \quad (9.7)$$

Because of $I_1(x) \geq \frac{x}{2}$ for $x \geq 0$ /13/, we find

$$D(\omega_n) \leq \frac{2}{\beta^2 \bar{R}} \quad (9.8)$$

and from this

$$|u(x,0)| \leq \sum D(\omega_n) |A_n| \leq \frac{2}{\beta^2 \bar{R}} \sum |A_n| \leq \frac{2}{\beta^2 \bar{R}} \sqrt{\frac{L}{\Delta S} \sum A_n^2} \quad (9.9)$$

where ΔS is the minimum path transducer preparation.

Use of the Parseval equation /33/

$$\sum A_n^2 \leq \frac{2}{L} \int_0^L \delta h^2(x) dx \leq 2C^2 \quad (9.10)$$

for

$$|\delta h(x)| \leq C \quad (9.11)$$

finally gives the simple estimation

$$|u(x,0)| \leq \frac{2}{\beta^2 \bar{R}} \sqrt{\frac{2L}{\Delta S}} C \quad (9.12)$$

If the maximum permissible remaining interference in the model region is given by

$$|u(x,0)| \leq \delta u \qquad (9.13)$$

then from (9.11) and (9.12) we obtain a tolerable contour error of

$$|\delta h(x)| \leq \frac{(1-M_\infty^2)\,\bar{R}}{2} \sqrt{\frac{\Delta S}{2L}}\,\delta u \qquad (9.14)$$

It can be seen that the adapted wall shape has to be adjusted more precisely with increasing incident flow mach number, which is physically understandable.

Quantitatively, for example, for $M_\infty = 0.7$, $\delta u = 0.006$ ($\bar{R} = 83$ mm, $\Delta S = 35$ mm, $L = 400$ mm) we have the accuracy requirement

$$|\delta h(x)| \leq 5 \cdot \delta u = 0.03 \text{ mm} \qquad (9.15)$$

which at least has a realistic order of magnitude.

10. A NEW METHOD FOR TESTING 3-D MODELS IN WIND TUNNELS WITH TWO FLEXIBLE WALLS

10.1 Introduction

Wind tunnels with two adaptive walls have been used for about ten years successfully for profile tests /4/. Therefore it is natural to also use these test facilities for testing three-dimensional models. Even though in this case one cannot achieve a completely interference free flow field in the test section by deflecting the upper and lower tunnel wall (for example, matching of porosity) one can attempt to at least reduce wall interferences in the model region.

This agrees with the idea that in order to avoid blocking effects it should be sufficient to produce a stream tube with the same cross-sectional area variation as is used for a complete three-dimensional wall adaptation. As Wedemeyer demonstrated with a numerical simulation, the resulting symmetric wall shape removes exactly the blocking speed on the tunnel axis /24/.

Based on this result, he developed a single step adaptation method. With it, by super position of one deflection and an opposite deflection of the two flexible test section walls, one can bring about an interference-free flow along the tunnel access $(x,\ y = \frac{h}{2},\ 0)$, Figure 22. (Symmetric models without slip angle are assumed.) The wall induced perturbation speeds $u_W(x,\ \frac{h}{2},\ 0)$ blocking and $v_W(x,\ \frac{h}{2},\ 0)$ (downwind) to be compensated for are then calculated using a singularity representation of the channel flow from the previously adjusted upper and lower wall contour and the prevailing pressure distributions there /25/.

The first experimental testing of this adaptation method was performed in the adaptive profile tunnels of the TUB and the ONERA/CERT /4/. A body of rotation at 0° incidence angle and a Canard model which produces lift (see Chapter 9) were tested. The pressure distribution measured along the top side of the body of revolution also agreed very well at high subsonic flow Mach numbers $(M_\infty = 0.84)$ with the corresponding interference-free values. This then confirms the possibility of already being able to essentially remove the blocking effect with a two-dimensional wall adaptation. In the more general case of flows with lift it was also possible to achieve a reduction of the perturbation speed, see Figure 20.

Based on the very low blocking ratios of 0.18% assumed, these results, however, only give conditional conclusions about the quality of the wall deflections calculated with the Wedemeyer program.

Independent of this, a theoretical analysis of the adaptation method in general leads to the conclusion of an increase in the remaining interferences with increasing model incidence angle. This is primarily due to the fact, that the wall influence is removed independent of the actual position of the investigated model, always along the tunnel axis.

In order to overcome this advantage, we will now introduce a new adaptation method based on the 3-D single step method, with which it is possible to do the following

(1) to exactly determine the wall influence in the test section;
(2) with which one can achieve an interference-free flow along the model axis.

The calculation of the interferences and the required wall displacement will be described in the following sections.

10.2 Determination of Wall Interferences in the 2-D Test Section

The wall induced perturbation speeds are obtained immediately by using the general representation formula (6.15) for the wall dependent potential, derived within the framework of the single step method

$$\phi_W(p) = -\frac{1}{4\pi\beta} \int_{S_1} \{v_A(q) - v_I(q)\}\, g(p,q)\, dq$$

$$g(p,q) = \{\frac{1}{\beta^2}(x_p-x_q)^2 + (y_p-y_q)^2 + (z_p-z_q)^2\}^{-\frac{1}{2}} \qquad (10.1)$$

$$\beta^2 = 1-M_\infty^2$$

where the control surface S_1 again corresponds to the test section geometry, Figure 22.

The normal speed distribution v_I is then determined in a known way by the variation of the upper and lower flexible walls and the two fixed side walls ($v_I = 0$) . The V_A-component is determined within the framework of an outer field calculation based on the measured wall pressure distribution (see Chapter 5). It is assumed that a measurement of the static pressure along the central lines of the two flexible walls and along the side wall is sufficient.

By differentiation of the relationship (10.1) we can then directly determine the perturbation speeds in the test section

$$u_W(p) = \frac{\partial \phi_W}{\partial x_p}(p)$$

$$v_W(p) = \frac{\partial \phi_W}{\partial y_p}(p) \qquad (10.2)$$

$$w_W(p) = \frac{\partial \phi_W}{\partial z_p}(p)$$

without any assumptions about the model-induced flow field (Chapter 6.1.2) directly from the measured wall pressures and the previously adjusted wall contour.

This procedure has the following advantages compared with the Wedemeyer procedure discussed above:

a calculation of the channel inner flow is not required. In this way, we avoid assumptions about the model-induced perturbations. The division into model effect in a symmetric displacement and asymmetric lift effect for

high model incidence angles used in this method of Wedemeyer is certainly only approximately valid.

The case of already deflected test section walls does not require any special calculations. In the Wedemeyer method on the other hand, the measured wall pressure distribution always has to be "corrected" on (aerodynamically) straight walls.

10.3 Calculation of the Adapted Wall Shape

10.3.1 Fundamental Remarks

By the deformation of the upper and lower flexible walls, the three-dimensional model flow in the test section is superimposed with a two-dimensional flow field. Let us assume small (additional) deflections

$$h_o(x) = \int_{-\infty}^{x} v(\xi,h)d\xi \qquad \text{(upper wall)}$$

$$h_u(x) = \int_{-\infty}^{x} v(\xi,0)d\xi \qquad \text{(lower wall)} \qquad (10.3)$$

Then the induced velocity field again can be assumed to be irrotational. The corresponding potential $\phi(x,y)$ then satisfies the following linear differential equation for subsonic flow

$$\beta^2\phi_{xx} + \phi_{yy} = 0 \ , \quad \beta^2 = 1 - M_\infty^2 \qquad (10.4)$$

with the boundary conditions defined by (10.3).

$$\frac{\partial\phi}{\partial y}(x,h) = v(x,h) =: v_o(x)$$

$$\frac{\partial\phi}{\partial y}(x,0) = v(x,0) =: v_u(x) \qquad (10.5)$$

The wall displacements $h_o(x)$ and $h_u(x)$ will then have to be determined so that the speeds which result from (10.4,5)

$$u(x,y) = \frac{\partial \phi}{\partial x}(x,y)$$

$$v(x,y) = \frac{\partial \phi}{\partial y}(x,y) \qquad (10.6)$$

will compensate for the wall interferences (10.2) as much as possible in the model region

$$(u_w + u)\Big|_{Model} \stackrel{!}{=} \min$$

$$(v_w + v)\Big|_{Model} \stackrel{!}{=} \min \qquad (10.7)$$

The components in the span direction w_w can apparently not be directly reduced. In the following we will therefore assume symmetric models without slip angle.

For the practical application of the 2-D wall adaptation, the physical requirements (10.7) however, have to be formulated so that the specified values of u and v will lead to an explicit calculation of the wall deflections $h_o(x)$ and $h_u(x)$. The condition which makes sense for this case is the following

$$u_w(x,y_M,0) + u(x,y_M) \stackrel{!}{=} 0$$

$$v_w(x,y_M,0) + v(x,y_M) \stackrel{!}{=} 0 \qquad (10.8)$$

where

$$y_M(x) = - x \tan\alpha + \frac{h}{2} \qquad (10.9)$$

is the model axis (Figure 22).

In the next section we will first calculate the adapted wall shape for the special case $\alpha = 0$ (model with no incidence).

10.3.2 Model at 0° Incidence Angle

For $\alpha = 0$ we wish to exactly cancel the interferences along the tunnel axis by deflecting the two-flexible test section walls according to (10.8)

$$u(x,\tfrac{h}{2}) \stackrel{!}{=} -u_w(x,\tfrac{h}{2},o) \quad \text{(Blockage)}$$

$$v(x,\tfrac{h}{2}) \stackrel{!}{=} -v_w(x,\tfrac{h}{2},o) \quad \text{(Downwind)} \qquad (10.10)$$

In order to calculate the required displacement paths $h_o(x)$, $h_u(x)$ we will start with the boundary value problem (10.4,5) and wish to establish an analytical relationship between $u(x,\frac{h}{2})$, $v(x,\frac{h}{2})$ and $v_o(x)$, $v_u(x)$.

For this purpose we will transform (10.4,5) using the usual coordinate transformation

$$x = \xi$$
$$y = \frac{1}{\beta}\eta \qquad (10.11)$$

into the equivalent incompressible flow problem

$$\frac{\partial^2 \tilde{\phi}}{\partial \xi^2} + \frac{\partial^2 \tilde{\phi}}{\partial \eta^2} = 0$$

$$\frac{\partial \tilde{\phi}}{\partial \eta}(\xi,\beta h) = \frac{1}{\beta} v_o(\xi) \qquad (10.12)$$

$$\frac{\partial \tilde{\phi}}{\partial \eta}(\xi,o) = \frac{1}{\beta} v_u(\xi)$$

By introducing the stream function $\tilde{\Psi}(\xi,\eta)$

$$\tilde{u}(\xi,\eta) = \frac{\partial \tilde{\phi}}{\partial \xi}(\xi,\eta) = \frac{\partial \tilde{\Psi}}{\partial \eta}(\xi,\eta)$$

$$\tilde{v}(\xi,\eta) = \frac{\partial \tilde{\phi}}{\partial \eta}(\xi,\eta) = -\frac{\partial \tilde{\Psi}}{\partial \xi}(\xi,\eta) \qquad (10.13)$$

it follows that

$$\tilde{\Psi}_{\xi\xi} + \tilde{\Psi}_{\eta\eta} = 0 \; ; \qquad -\infty < \xi < +\infty \; ; \; 0 \leq \eta \leq \beta h$$

$$\tilde{\Psi}(\xi,\beta h) = -\frac{1}{\beta}\int_{-\infty}^{\xi} v_o(t)dt = -\frac{1}{\beta} h_o(\xi) \qquad (10.14)$$

$$\tilde{\Psi}(\xi,0) = -\frac{1}{\beta}\int_{-\infty}^{\xi} v_u(t)dt = -\frac{1}{\beta} h_u(\xi)$$

The Dirichlet problem (10.14) occurs in a similar form also in connection with two-dimensional wall interference correction procedures, so that we can derive the solution from the appropriate references /26,27/. For the speeds induced along the tunnel axis we obtain the following clear relationships /26/

$$\tilde{u}(\xi,\frac{\beta h}{2}) = \frac{\partial \tilde{\Psi}}{\partial \eta}(\xi,\frac{\beta h}{2}) = -\frac{1}{\beta^2 h}\int_{-\infty}^{+\infty} \frac{v_o(t)-v_u(t)}{1+e^{\frac{2\pi(t-\xi)}{\beta h}}}dt$$

$$\tilde{v}(\xi,\frac{\beta h}{2}) = -\frac{\partial \tilde{\Psi}}{\partial \xi}(\xi,\frac{\beta h}{2}) = \frac{1}{\beta^2 h}\int_{-\infty}^{+\infty} \frac{v_u(t)+v_o(t)}{2\cosh\frac{\pi(t-\xi)}{\beta h}}dt \qquad (10.15)$$

A reverse transformation into the x,y-plane, because of

$$\tilde{u}(\xi,\frac{\beta h}{2}) = u(x,\frac{h}{2})$$

$$\tilde{v}(\xi,\frac{\beta h}{2}) = \frac{1}{\beta} v(x,\frac{h}{2}) \qquad (10.16)$$

gives the following coupled integral equations for calculating the adaptive wall shape

$$u(x,\frac{h}{2}) = -\frac{1}{\beta^2 h}\int_{-\infty}^{+\infty}\frac{v_o(t)-v_u(t)}{1+e^{\frac{2\pi(t-x)}{\beta h}}}\,dt \stackrel{!}{=} -u_w(x,\frac{h}{2},o)$$

$$v(x,\frac{h}{2}) = \frac{1}{\beta h}\int_{-\infty}^{+\infty}\frac{v_o(t)+v_u(t)}{2\cosh\frac{\pi(t-x)}{\beta h}}\,dt \stackrel{!}{=} -v_w(x,\frac{h}{2},o) \qquad (10.17)$$

The numerical solution of (10.17) poses no difficulties and then immediately leads to the desired deflections by subsequent integration of v_u and v_o .

As expected, in order to compensate for the blocking speed, one requires a wall deformation which is symmetric with respect to the tunnel action (cross-section change). In the case of models with lift, in addition one has to displace the test section cross-section parallel in the rear region (asymmetric deflection).

As already mentioned in Section 10.1, this result was already achieved before by Wedemeyer /25/. However, his calculation of the adapted wall contour in the form of a series expansion is less favorable than the exact solution (10.17).

10.3.3 Models with Incidence

With increasing incidence angle α the models move away from the tunnel central line. Therefore it is more accurate to remove the wall interferences along the model axis (see (10.8.9)). The calculation of the deflections required for this can then be done in many ways.

With boundary value problem (10.14) in general, a relationship is established between a wall contour change and the subsequent induced velocities in the test section. As Mokry shows, it can be solved in closed form by separating the variables (Fourier method) /27/

$$\Psi(\xi,\eta) = f(\xi,\eta;\ a_1,\ a_2,\ \ldots,\ b_1,\ b_2,\ \ldots) \qquad (10.18)$$

where a_i and b_i are the Fourier coefficients from the (formal) expansions for $h_o(\xi)$ and $h_u(\xi)$. In order to determine these constant desired wall displacements, apparently one can again prescribe $\frac{\partial \hat{\Psi}}{\partial \xi}$ and $\frac{\partial \hat{\Psi}}{\partial \eta}$ along the symmetry axis or any other line in the tunnel. This procedure for example has been investigated within the framework of a study paper /28/.

On the other hand, one can start with the exact relationships (10.17) for $\alpha = 0$ and from this obtain an approximate solution for $\alpha \neq 0$ using a Taylor series expansion for $u(x,y_M(x))$ and $v(x,y_M(x))$.

$$
\begin{aligned}
u(x,y_M(x)) &= u(x,\tfrac{h}{2}) - x \tan \alpha\, u_y\,(x,\tfrac{h}{2}) \\
&\quad + \frac{x^2\tan^2\alpha}{2}\, u_{yy}\,(x,\tfrac{h}{2}) \mp \cdots \\
&= u(x,\tfrac{h}{2}) - x \tan \alpha\, v_x\,(x,\tfrac{h}{2}) \\
&\quad - \frac{\beta^2 x^2\tan^2\alpha}{2}\, u_{xx}\,(x,\tfrac{h}{2}) \pm \cdots
\end{aligned}
\qquad (10.19)
$$

$$
\begin{aligned}
v(x,y_M(x)) &= v(x,\tfrac{h}{2}) + \beta^2\, x \tan \alpha\, u_x\,(x,\tfrac{h}{2}) \\
&\quad - \frac{\beta^2 x^2\tan^2\alpha}{2}\, v_{xx}\,(x,\tfrac{h}{2}) \mp \cdots
\end{aligned}
$$

and in order to replace the derivatives with respect to y one uses the equations

$$
\begin{aligned}
\beta^2 u_x + v_y &= 0 \qquad \text{(continuity)} \\
u_y - v_x &= 0 \qquad \text{(irrotationality)}
\end{aligned}
\qquad (10.20)
$$

If we now introduce the abbreviations

$$v_1(t) = v_u(t) - v_o(t)$$

$$v_2(t) = v_u(t) + v_o(t)$$

$$K_1(t-x) = \frac{1}{\beta^2 h} \quad \frac{1}{1+e^{\frac{2\pi(t-x)}{\beta h}}} \tag{10.21}$$

$$K_2(t-x) = \frac{1}{\beta h} \quad \frac{1}{2\cosh\frac{\pi(t-x)}{\beta h}}$$

then the adapted wall shape

$$h_o(x) = \frac{1}{2} \int_{-\infty}^{x} \{v_2(t) - v_1(t)\}\, dt$$

$$h_u(x) = \frac{1}{2} \int_{-\infty}^{x} \{v_2(t) + v_1(t)\}\, dt \tag{10.22}$$

finally results by replacing (10.17) in (10.19)

$$\int_{-\infty}^{+\infty} v_1(t)\, K_1(t-x)dt - x\tan\alpha \int_{-\infty}^{+\infty} v_2(t)\, \frac{d}{dx} K_2(t-x)dt$$

$$- \frac{\beta^2 x^2 \tan^2\alpha}{2} \int_{-\infty}^{+\infty} v_1(t)\, \frac{d^2}{dx^2} K_1(t-x)dt \pm \cdots \tag{10.23}$$

$$\stackrel{!}{=} - u_w(x, y_M(x), 0)$$

$$\int_{-\infty}^{+\infty} v_2(t)\, K_2(t-x)dt + \beta^2 x\tan\alpha \int_{-\infty}^{+\infty} v_1(t)\frac{d}{dx}K_1(t-x)dt$$

$$- \frac{\beta^2 x^2 \tan^2\alpha}{2} \int_{-\infty}^{+\infty} v_2(t)\frac{d^2}{dx^2} K_2(t-x)dt \mp \cdots$$

$$\stackrel{!}{=} - v_w(x, y_M(x), 0)$$

For $\alpha = 0$ (10.23) of course reduces to solution (10.17). The number of terms to be considered for $\alpha \neq 0$ has to be determined by experiment. The linear equation system which approximates (10.23) always has the form

$$A\,\vec{v}_1 + B\,\vec{v}_2 = -\vec{u}_w$$

$$C\,\vec{v}_1 + D\,\vec{v}_2 = -\vec{v}_w \qquad (10.24)$$

and can easily be solved by inversion

$$\begin{pmatrix} \vec{v}_1 \\ \vec{v}_2 \end{pmatrix} = - \begin{pmatrix} A & B \\ C & D \end{pmatrix}^{-1} \begin{pmatrix} \vec{u}_w \\ \vec{v}_w \end{pmatrix} \qquad (10.25)$$

11. SUMMARIES

The ever increasing requirements for quality of wind tunnel results in high subsonic flows led to the development of so-called "adaptive" test sections around 1970. One uses the natural idea of removing the cause of wall interferences by matching the test section walls through the side ways unlimited model flow.

After the use of this new technology for profile tests, in 1979 we started building three-dimensional adaptive test sections. Out of the three realized designs, the special construction features of the octagon test section with eight flexible walls has been discussed in detail which was built at the TU Berlin.

After this, we gave a detailed discussion of the newly developed numerical methods for 3-D wall adaptation developed here. Starting with conventional iteration adaptation methods, we first investigate the three-dimensional design path (outer field calculation) which has to be solved at each regulation step. Using a

simple perturbation calculation, the ill-posedness of this inverse problem is demonstrated. Then we introduced the design method developed to solve this problem. In this, the desired wall shape is calculated directly from the prescribed pressure distribution, but instead by stepwise modification of an initial contour. The required geometric changes are determined using a design rule from the difference between the actual and nominal pressure distribution. Each of the actual values can be determined with the panel or the TSP method as desired. The post calculation task can be solved numerically without problems and in the linear case can be reduced to a simple matrix vector multiplication. The design method therefore does not only allow a simple check of the calculated wall deflections, but has addition numerical advantages.

Use of the iteration wall adaptation method with the prescribed outer field calculation method in 1982 gave the basic functional proof of the octagon test section. But in order to regulate the eight flexible walls, in general more than ten intermediate steps were necessary even after matching up the regulation factor which determines conversion.

In order to make a systematic investigation of the adaptation behavior, we performed a numerical simulation. The wall pressure distribution in the individual regulation steps is not determined by a wind tunnel test, but using physically reasonable assumptions about the given wall contour, This numerical study did not only verify the experimental results, but also shows that even if one uses an optimum regulation factor, one can not achieve fast conversions.

In a further theoretical analysis, the allowable regulation range finally was determined exactly. It is found that the iteration 3-D wall adaptation method diverges theoretically for all regulation factors. The conversions found in practical

wind tunnel tests or in numerical simulations are only caused by the (inaccurate) numerical approximation of the boundary conditions!

On the otherhand, using the relationships derived during the simulation for the channel inner flow, we were able to establish a basic formula for the wall dependent perturbation potential in the subsonic case. This allows a calculation of the interferences in the test section based on the known wall contour and the prevailing pressure distribution. A representation of the model flow is not required.

Use of this formula leads directly to a single step adaptation method. The calculation of the adapted wall contour from the wind tunnel measured values is then possibly based on a simple linear relationship. As a comparison with the iteration method shows, the single step formula is found formally by replacing the constant regulation factor by a matrix which considers the incident flow mach number and the test section geometry. In the case of flow near the speed of sound or very large wall interferences, the assumptions used in this formulation, however, only apply approximately, so that in these cases several adaptation steps may be necessary.

An experimental testing of the single step adaptation method in the octagon test section then clearing confirms the assumed fast conversions. The wall contour in general was already adapted after two regulation steps in general. We use the change in the data measured on the model as the truncation criterion. The high quality of the adjusted wall shape is demonstrated as an example for a tested model (Canard configuration) for a incident Mach number $M_\infty = 0.7$ using interference-free comparison measurements.

The outer field calculation required in any adaptation step was always performed using the subsonic panel method during the testing, in order to save calculation time. It was only in one flow case, where the local supersonic regions extended to the test section walls, that one could not achieve a reliable adaptation. A comparison calculation with the TSP program then resulted in a somewhat different wall deflection for the first adaptation step. After improvement of the poor flow quality which occurs for incident flow near the speed of sound in the model test section, one should then perform a complete wall adaptation with the TSP method.

At the conclusion of this paper we then developed a new method for testing three-dimensional models in wind tunnels with two flexible walls. By using the already mentioned general representation formula for the wall dependent perturbation potential, one can then calculate the interferences in the test section without any additional assumptions about the model induced flow field. It is shown that by a suitable deflection of the upper and lower flexible walls, one can always remove the perturbation speeds along the model axis. The adapted wall shape for models with incidence is then determined from a series expansion from the deflections for $\alpha = 0$.

REFERENCES

[1]	Ferri, A., Baronti, P.	A Method for Transonic Wind Tunnel Corrections AIAA Journal, Vol. 11, No 1 (1973)
[2]	Sears, W. R.	Self Correcting Wind Tunnels The Sixteenth Lanchester Memorial Lecture, London, Mai 1973 Calspan Rep. RK - 5070-A-2, Juli 1973 The Aeronautical Journal, Vol. 78 (1974)

| 3| Jaswon, M.A., Symm, G. T. — Integral Equation Methods in Potential Theory and Elastostatics. Academic Press; London, New York, San Francisco, 1977

| 4| Ganzer, U. — A Review of Adaptive Wall Wind Tunnels. Progress in Aerospace Science, Vol 22. Pergamon Press, Oxford 1985

| 5| Parker, R. L., Erickson, J. C. — Development of a Three-Dimensional Adaptive Wall Test Section with Perforated Walls. AGARD-CP-335, Mai 1982

| 6| Parker, R.L., Erickson, J. C. — Status of Three-Dimensional Adaptive-Wall Test Section Development at AEDC. AIAA Paper No. 84-0624, März 1984

| 7| Heddergott, A., Wedemeyer, E. — Deformable Adaptive Wall Test Section for Three-Dimensional Wind Tunnel Testing. ICAS Paper 84-2.1.2, Sept. 1984

/8/ Ganzer, U., Igeta, Y., Kleemann, E., Rebstock, R. — Development of an adaptive wind tunnel test section with flexible walls for three-dimensional transonic flows. BMFT-FB-W 83-026, October, 1983.

| 9| Moses, D.F. — Wind Tunnel Wall Corrections Deduced by Iterating from Measured Wall Static Pressure. AIAA Journal Vol 21, No. 12, Dezember 1983

|10| Spee, B. M., Yoshihara, H. (Herausgeber) Applied Computational Transonic Aerodynamics AGARDograph No. 266 (1982)

|11| Wang, Shu-Chieh Convergence to Unconfined Flow of the Three-Dimensional Transonic Self-Correcting Wind Tunnel Computer Methods in Applied Mechanics and Engineering, No. 28 (1981)

/12/ Wehlitz, Pamela Design methods for determining the wall shape in three-dimensional adaptive test sections with flexible walls. Study paper at the ILR, TU Berline 1984.

|13| Abramowitz, M., Stegun, I.A. (Herausgeber) Handbook of Mathematical Functions Dover Publications, Inc. New York 1970

/14/ Zierep, J. Theoretical Gas Dynamics, Karlsruhe, Braun 1976.

|15| Ganzer, U., Igeta, Y., Ziemann, J. Design and Operation of TU Berlin Wind Tunnel with Adaptable Walls ICAS Paper 84-2.1.1, September 1984

|16| Atkinson, K.E. An Introduction to Numerical Analysis John Willey & Sons, New York 1978

|17| Hess, J.L., Smith, A.M.O. Calculation of Potential Flow about Arbitrary Bodies Progress in Aeronauticel Sciences Vol 8 Pergamon Press, London, New York, Paris 1967

|18| Murman, E.M., Cole, J. D. — Calculation of Plane Steady Transonic Flows AIAA Journal Vol 9, No. 1 (1971)

/19/ Rill, Stefan — Calculation of Wind Tunnel Wall Inteferences by Simulation of the Regulation Method for Three-Dimensional Adaptive Test Sections. Diplomathesis at the ILR, TU Berlin, 1984.

/20/ Mokry, M. — Higher Analysis. VEB Deutscher Verlag der Wissenschaften, Berlin 1972

|21| Mokry, M. — Subsonic Wall Interference Corrections For Finite-Length Test Sections Using Boundary Pressure Measurements AGARD-CP-335, Mai 1982

|22| Rebstock, R. — Numerical Methods for Adapting Wind Tunnel Walls ILR-Mitt. 144, TU Berlin 1984

/23/ Spath, H. — Spline-Algorithms for Construction of Smooth Curves and Surfaces. R. Oldenbourg Verlag, Muenchen, Wien, 1973

|24| Wedemeyer, E. — The Computer in Experimental Fluid Dynamics Lecture Series 1985-06 Von Karman-Institute For Fluid Dynamics 1985

|25| Wedemeyer, E. — Wind Tunnel Testing of Three Dimensional Models in Wind Tunnels with Two Adaptive Walls Preprint 1982-36 Von Karman-Institute For Fluid Dynamics 1982

/26/ Capelier, C., Chevallier, J.P., Bouniol, F.
New correction method of the wall effect in plane flow. La Recherche Aerospatiale, No. 1978-1 (1978)

|27| Mokry, M., Ohman, L.H.
Application of the Fast Fourier Transform to Two-Dimensional Wind Tunnel Wall Interference Journal of Aircraft, Vol 17, No. 6 (1980)

/28/ Lehmann, Dirk
3D-Model investigations in wind tunnels with two flexible walls --Numerical methods for wall adaptation-- Study paper at the ILR, TU Berlin 1986

/29/ Ganzer, U., Rebstock, R.
Flexible adaptive walls for transonic wind tunnels in the subsonic and supersonic flows, DGLR-Paper Nr. 84-108, 1984

|30| Ganzer, U.
On the Use of Adaptive Walls for Transonic Wind Tunnel Testing AGARD-CP-335, Mai 1982

/31/ Kuczka, D.
DFVLR-Gottingen, Institute for Experimental Fluid Mechanics Private Communication

/32/ Igeta, Y.
3D-Model investigations in a test section with eight flexible walls. Internal Report, ILR, TU Berlin, 1986

/33/ Bronstein, I., Semendjajew, K.
Handbook of Mathematics. Teubner Verlagsgesellschaft 1972

|34| Holt, D.R. Hunt, B.
The Use of Panel Methods for the Evaluation of Subsonie Wall Interference AGARD-CP-335 Mai 1982

13. APPENDIX

13.1 Calculation of the Influence Coefficients

Using the abbreviation

$$\phi_{ij} = -\frac{1}{4\pi\beta} \int_{\Delta_j} g(p_i,q)\,dq$$

the following is obtained for the influence coefficients (Formulas (5.31) and (5.36)) in the body-fixed (x,y,z)-coordinate system, Figure 9

$$A_{ij} = \frac{\partial}{\partial n_i}\phi_{ij} = \vec{n_i} \cdot \nabla\phi_{ij} = n_{i,y}\frac{\partial}{\partial y}\phi_{ij} + n_{i,z}\frac{\partial}{\partial z}\phi_{ij}$$

$$B_{ij} = \frac{\partial}{\partial x}\phi_{ij}$$

The calculation of $\nabla\phi_{ij}$ is done however, in the panel-related system (x', y', z') in the most simple way

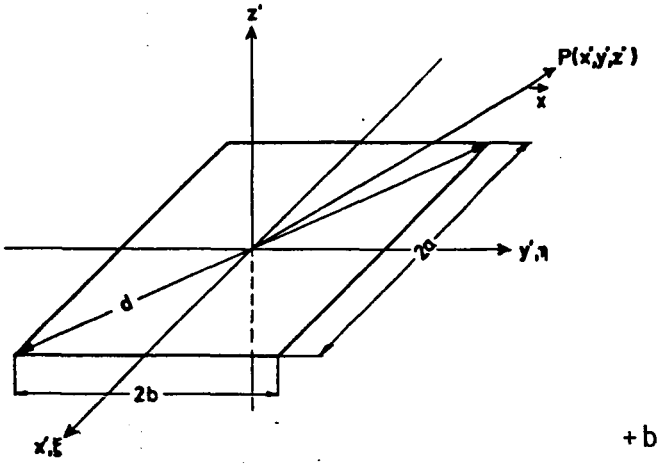

$$\phi(\vec{x'}) = -\frac{1}{4\pi\beta} \int_{-b}^{+b} \int_{-a}^{+a} \frac{1}{\sqrt{\frac{1}{\beta^2}(x'-\xi)^2+(y'-\eta)^2+z'^2}}\,d\xi d\eta$$

The reverse transformation into the body-fixed coordinates is then given by

$$\frac{\partial \phi}{\partial x} = \frac{\partial \phi}{\partial x'}$$

$$\frac{\partial \phi}{\partial y} = n_{z,j} \frac{\partial \phi}{\partial y'} + n_{y,j} \frac{\partial \phi}{\partial z'}$$

$$\frac{\partial \phi}{\partial z} = - n_{y,j} \frac{\partial \phi}{\partial y'} + n_{z,j} \frac{\partial \phi}{\partial z'}$$

Depending on the distance between the target point P and the induced panel, after this three different formula collections are used for the perturbation speeds. The range of validity was limited as follows according to a suggestion by Hess and Smith /17/ (see Figure above)

$\left|\frac{\vec{x}'}{d}\right| \leq 2.45$ exact formulas

$2.45 < \left|\frac{\vec{x}'}{d}\right| \leq 4$ multipole expansion up to including quadrupole term

$\left|\frac{\vec{x}'}{d}\right| > 4$ source approximation

In the first two cases, the already mentioned transformation into the panel coordinate system is required. Exact formulas:

With the abbreviations

$$d = \{\frac{1}{\beta^2} (x'-a)^2 + (y'+b)^2 + z'^2\}^{\frac{1}{2}}$$

$$e = \{\frac{1}{\beta^2} (x'+a)^2 + (y'+b)^2 + z'^2\}^{\frac{1}{2}}$$

$$f = \left\{\frac{1}{\beta^2}\,(x'-a)^2 + (y'-b)^2 + z'^2\right\}^{\frac{1}{2}}$$

$$g = \left\{\frac{1}{\beta^2}\,(x'+a)^2 + (y'-b)^2 + z'^2\right\}^{\frac{1}{2}}$$

We find

$$\frac{\partial \phi}{\partial x'}\,(x',y',z') = \frac{1}{4\pi\beta}\left\{\ln\frac{y'+b+d}{y'-b+f} - \ln\frac{y'+b+e}{y'-b+g}\right\}$$

$$\frac{\partial \phi}{\partial x'}\,(0,0,0) = 0.$$

$$\frac{\partial \phi}{\partial y'}\,(x',y',z') = \frac{1}{4\pi}\left(\ln\frac{x'+a+\beta g}{x'-a+\beta f} - \ln\frac{x'+a+\beta e}{x'-a+\beta d}\right)$$

$$\frac{\partial \phi}{\partial y'}\,(0,0,0) = 0.$$

$$\frac{\partial \phi}{\partial z'}\,(x',y',z') = \frac{1}{4\pi}\,\mathrm{sign}\,(z')\,\{\mathrm{sign}\,(x'+a)\cdot \left[\arctan\frac{|x'+a|\,(y'+b)}{|z'|\,\beta e} - \arctan\frac{|x'+a|\,(y'-b)}{|z'|\,\beta g}\right] - \mathrm{sign}\,(x'-a)\left[\arctan\frac{|x'-a|\,(y'+b)}{|z'|\,\beta d} - \arctan\frac{|x'-a|\,(y'-b)}{|z'|\,\beta f}\right]\}$$

$$\frac{\partial \phi}{\partial z'}\,(0,0,0) = \frac{1}{2}$$

Multipole expansion:

Since the coordinate origin is at the panel center of gravity, no dipole term results. With the separation

$$r_o = \sqrt{\left(\frac{x'}{\beta}\right)^2 + y'^2 + z'^2}$$

it follows that

$$\frac{\partial \phi}{\partial x'}(x',y',z') = -\frac{1}{4\pi\beta}\left\{x' 4ab\left[-\frac{1}{r_o^3}+\frac{1}{2\beta^2}\,\frac{3a^2+b^2\beta^2}{r_o^5}\right.\right.$$
$$\left.\left.-\frac{5}{2\beta^4}\,\frac{(ax')^2+(\beta^2 by')^2}{r_o^7}\right]\right\}$$

$$\frac{\partial \phi}{\partial y'}(x',y',z') = -\frac{1}{4\pi\beta}\left\{y' 4ab\left[-\frac{1}{r_o^3}+\frac{1}{2\beta^2}\,\frac{a^2+3b^2\beta^2}{r_o^5}\right.\right.$$
$$\left.\left.-\frac{5}{2\beta^4}\,\frac{(ax')^2+(\beta^2 by')^2}{r_o^7}\right]\right\}$$

$$\frac{\partial \phi}{\partial z'}(x',y',z') = -\frac{1}{4\pi\beta}\left\{z' 4ab\left[-\frac{1}{r_o^3}+\frac{1}{2\beta^2}\,\frac{a^2+b^2\beta^2}{r_o^5}\right.\right.$$
$$\left.\left.-\frac{5}{2\beta^4}\,\frac{(ax')^2+(\beta^2 by')^2}{r_o^7}\right]\right\}$$

Source approximation:

In the body-fixed reference system we assume that the panel center of gravity has the coordinates (x_o, y_o, z_o) and the target point is given by (x,y,z).

Using

$$\tilde{r}_o = \sqrt{\frac{1}{\beta^2}(x-x_o)^2 + (y-y_o)^2 + (z-z_o)^2}$$

we find that

$$\frac{\partial \phi}{\partial x}(x,y,z) = -\frac{1}{4\pi\beta}\left[\frac{4ab}{\beta^2}\,\frac{x_o-x}{\tilde{r}_o^3}\right]$$

$$\frac{\partial \phi}{\partial y}(x,y,z) = -\frac{1}{4\pi\beta}\left[4ab\,\frac{y_o-y}{\tilde{r}_o^3}\right]$$

$$\frac{\partial \phi}{\partial z}(x,y,z) = -\frac{1}{4\pi\beta}\left[4ab\,\frac{z_o-z}{\tilde{r}_o^3}\right]$$

Influence coefficients A_{ij} for $M_\infty \to 1$ ($\beta \to 0$)

For $M_\infty \to 1$ the upstream and downstream effects of the induced panels vanish. The speeds induced in the circumferential direction are

$$\frac{\partial \phi}{\partial y'} (0,y',z') = -\frac{1}{4\pi} \ln \frac{(y'-b)^2+z'^2}{(y'+b)^2+z'^2}$$

$$\frac{\partial \phi}{\partial z'} (0,y',z') = -\frac{1}{2\pi} \operatorname{sign}(z') \left\{ \operatorname{arc\,tg} \frac{y'-b}{|z'|} - \operatorname{arc\,tg} \frac{y'+b}{|z'|} \right\}, \quad z' \neq 0$$

$$\frac{\partial \phi}{\partial z'} (0,0,0) = \frac{1}{2}$$

13.2 Analytical Investigation of the Conversions of the Iterative Wall Adaptation Method

We will start with the iteration scheme (3.3)

$$\left.\begin{aligned} v_A^{(n)} &= v_A\left[u_I^{(n)}\right] \\ v_I^{(n+1)} &= v_I^{(n)} + K\left(v_A^{(n)} - v_I^{(n)}\right), \quad K \in (0,1) \end{aligned}\right\} n = 1,2,\ldots \quad (13.1)$$

and we will define the increments

$$\begin{aligned} \delta u_I^{(n+1)} &= u_I^{(n+1)} - u_I^{(n)} \\ \delta v_I^{(n+1)} &= v_I^{(n+1)} - v_I^{(n)} = K\left(v_A^{(n)} - v_I^{(n)}\right) \end{aligned} \quad (13.2)$$

The purpose of the following analysis is to establish a recursion formula for the δv_I .

$$\begin{aligned} \delta v_I^{(n+2)} &= K\,(v_A^{(n+1)} - v_I^{(n+1)}) \\ &= K\,(v_A^{(n)} + v_A\,[\delta u_I^{(n+1)}] - v_I^{(n)} - \delta v_I^{(n+1)}) \\ &= (1-K)\,\delta v_I^{(n+1)} + K v_A\,[\delta u_I^{(n+1)}] \end{aligned} \qquad (13.3)$$

Using relationships (6.12)-(6.14) we then find

$$v_A[\delta u_I^{(n+1)}] = A\sigma = A(v_A[\delta u_I^{(n+1)}] - \delta v_I^{(n+1)}) \qquad (13.4)$$

and from this

$$A' v_A[\delta u_I^{(n+1)}] = - A\delta v_I^{(n+1)} \qquad (13.5)$$

(13.3) and (13.5) give the important intermediate result

$$A'\delta v_I^{(n+2)} = \{A'-K(A+A')\}\,\delta v_I^{(n+1)} = (A'-KE)\,\delta v_I^{(n+1)}, \qquad n = 1,2,... \qquad (13.6)$$

The iteration rule (13.6) apparently can be carried out exactly uniquely when the free constant in the solution collection of A' is suppressed, i.e. we only consider the subspace

$\delta v_I^{(n+1)} \varepsilon R_o^{\perp} = R^{\underset{\sim}{N}} C\vec{e}$ C=konst., $\vec{e} = (1,1,...,1)$, $n = 1,2,...$;

This additional assumption amounts to $v_A^{(n)} \varepsilon R_o^{\perp}$ because of (13.2). This only means that out of the first incident number of solutions $v_A[\delta u_I^{(n+1)}]$ "physically correct" solution $v_A[\delta\phi^{(n+1)}]$ has to be taken (see Chapter 5.1).

Since A' of the subspace $R_o^{\perp}$ can be inverted, using the abbreviation $A'|_{R_o^{\perp}} = \hat{A}'$ from (13.6) we find the desired recursion relationship

$$\delta v_I^{(n+2)} = (E-K\hat{A}'^{-1})\delta v_I^{(n+1)} = (E-K\hat{A}'^{-1})^n \delta v_I^{(2)}, \qquad (13.7)$$

$$n = 1,2,...$$

with which one can then investigate the conversion properties of (13.1). Because of

$$\delta v_I^{(n+2)} \to 0 \iff (E-K\hat{A}'^{-1})^n \to 0 \text{ (0 Matrix)} \qquad (13.8)$$

then according to a well known mathematical theorem /16/, (13.1) converges. Then the following estimation applies for the spectral radius of the iteration matrix $G = E - K\hat{A}'^{-1}$

$$\zeta(G) = \max_{1\leq i\leq N-1} |\lambda_i| < 1 \qquad (13.9)$$

The Eigen values λ_i of G are

$$\lambda_i = 1 - K\mu_i \quad , \quad i = 1,...,N-1 \qquad (13.10)$$

where $\upsilon_i = \frac{1}{\mu_i}$ are the Eigen values of $\hat{A}'$.

According to the theorem of Gerschgorin /16/ we have the following inequality for the υ_i

$$|\upsilon_i - \tfrac{1}{2}| \leq \tfrac{1}{2} \quad , \quad i = 1, ..., N-1 \qquad (13.11)$$

(This follows from (6.6), (6.8), (6.9) and the fact that the υ_i are also Eigen values of A).

From (13.11) we find $\mathrm{Re}(\upsilon_i)>0$ and therefore the following conversion theorem follows.

Let $\upsilon_M = Re(\upsilon_M) + iIm(\upsilon_M)$ be the Eigen value of $\hat{A}'$ with the smallest real part. Then the iteration procedure (13.1) converges exactly for all K with

$$0 < K < 2Re(\upsilon_M) \qquad (13.12)$$

Proof:

From (13.10) it follows that

$$|\lambda_i|^2 = \lambda_i \bar{\lambda}_i = (1-K\mu_i)(1-K\bar{\mu}_i) = 1-2KRe(\mu_i)+K^2|\mu_i|^2$$

$$= 1-2K\frac{Re(\nu_i)}{|\nu_i|^2} + K^2\frac{1}{|\nu_i|^2} = 1 - \frac{2KRe(\nu_i)-K^2}{|\nu_i|^2}$$

and therefore because of

$$|\lambda_i|^2 < 1 <=> 2KRe(\nu_i) - K^2 > 0 , \quad i=1,\cdots,N-1 \qquad (13.13)$$

the theorem is immediately proven.

The matrix $\hat{A}'$ is a discrete form of the integral operator (6.3) (restricted to the partial space of the functions which are not constant on S). One then has to ask how ν_M and therefore the magnitude of the permissible regulation range $2Re(\nu_M)$ depends on the selected paneling.

From literature we can derive the general fact that Fredholm integral equations of the second kind have an infinite number of Eigen values, which can at the most accumulate at the origin /20/. In our case the Eigen values (6.3) are also restricted (estimation (13.11) applies also for the continuous operator). Therefore they have to have an accumulation point (theorem of Bolzano-Weierstrass). Therefore we have

$$Re(\nu_M) \to 0 \quad \text{for} \quad N \to \infty \qquad (13.14)$$

and therefore using (13.12) we find

$$K \to 0 \quad \text{for} \quad N \to \infty \tag{13.15}$$

The conversion of the iteration method (13.1) deteriorates as the accuracy of the inner and outer field calculation increases. It even fails completely in the case of infinitely fine paneling!

The "conversions" found during practical wind tunnel testing or during numerical simulation therefore are only caused by the inaccurate numerical approximation of the boundary conditions!

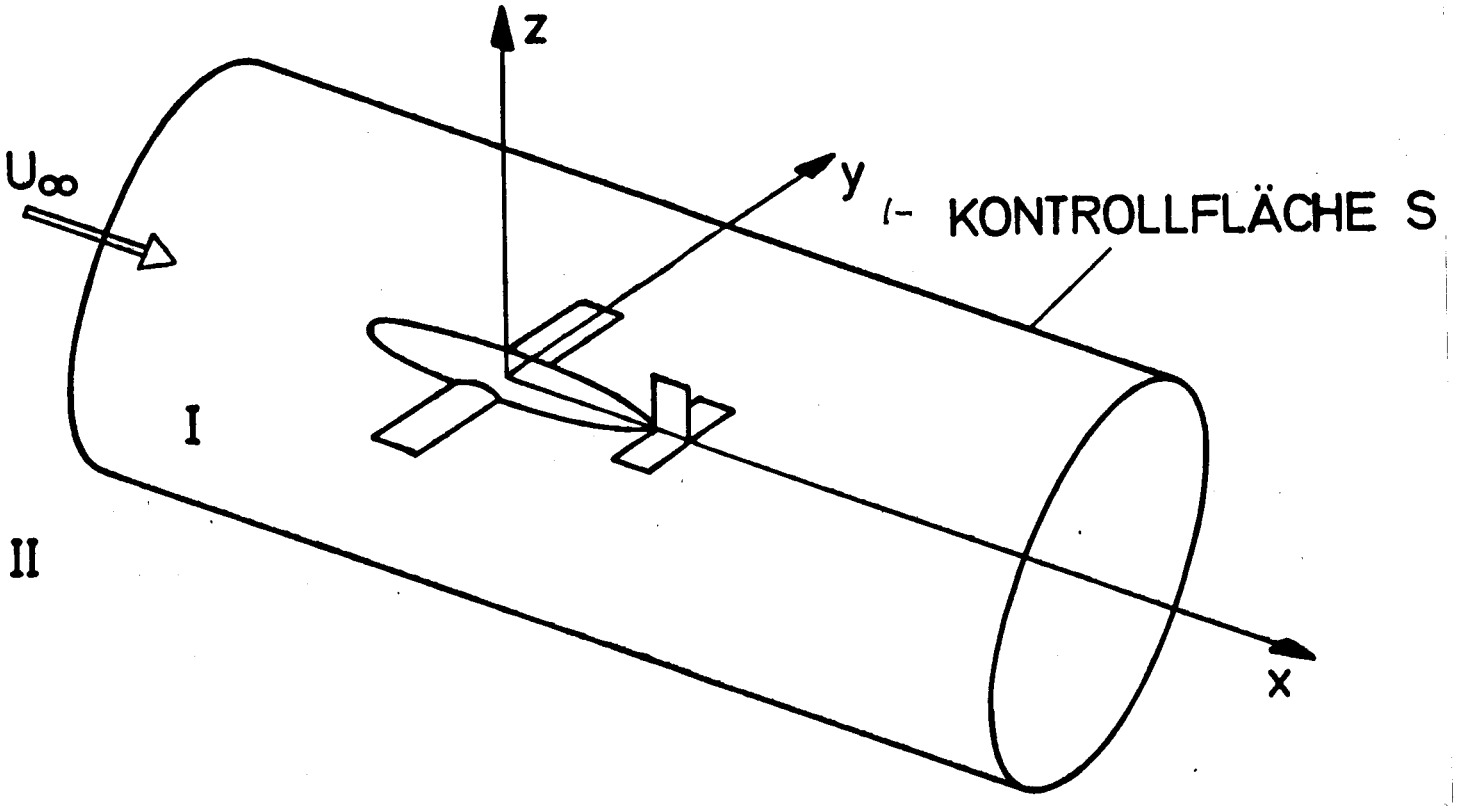

Figure 1. Flow Regions for 3D Model Flow.
Key: 1) control surface S.

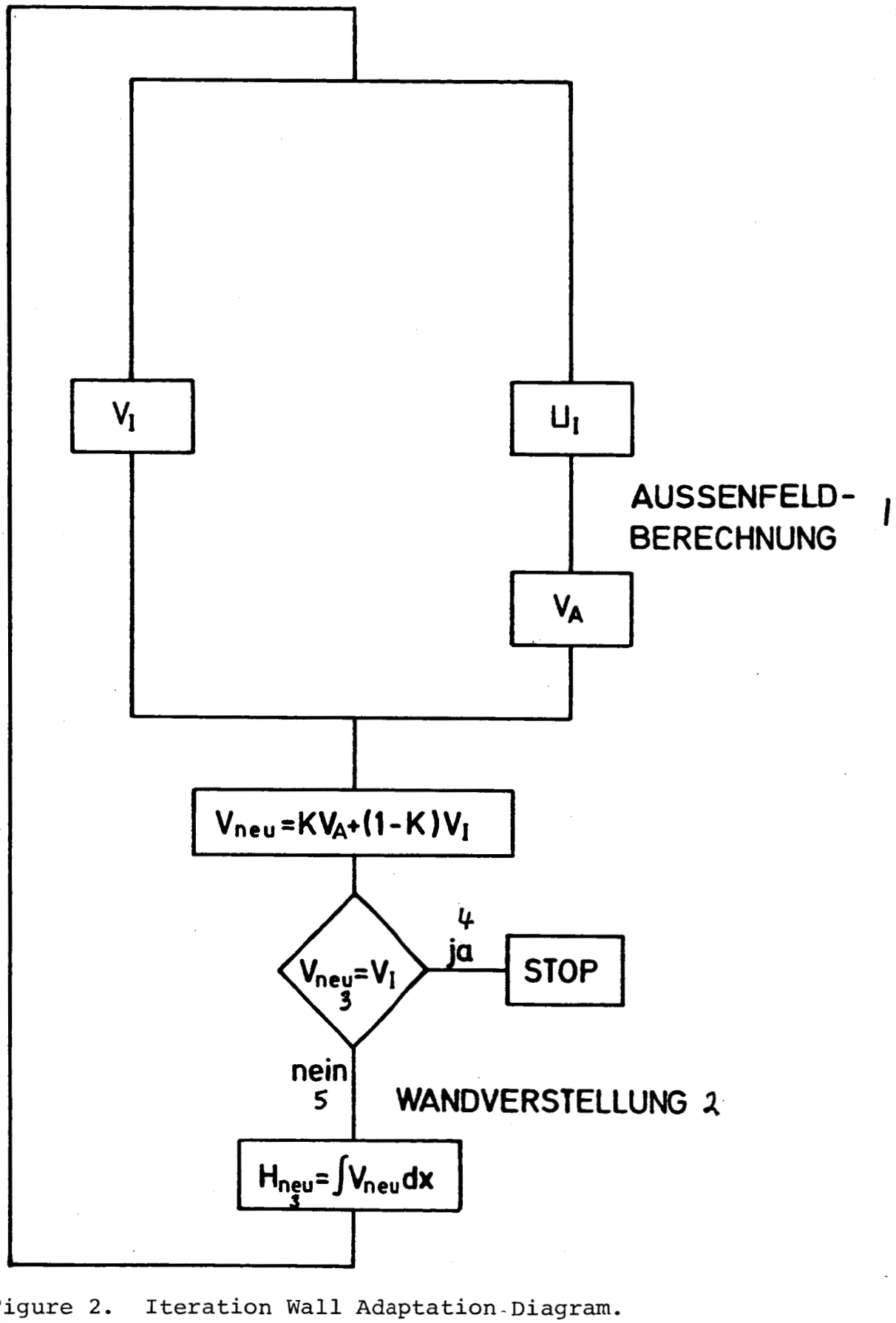

Figure 2. Iteration Wall Adaptation Diagram.

Key: 1) outer field calculation; 2) wall displacement; 3) new; 4) yes; 5) no.

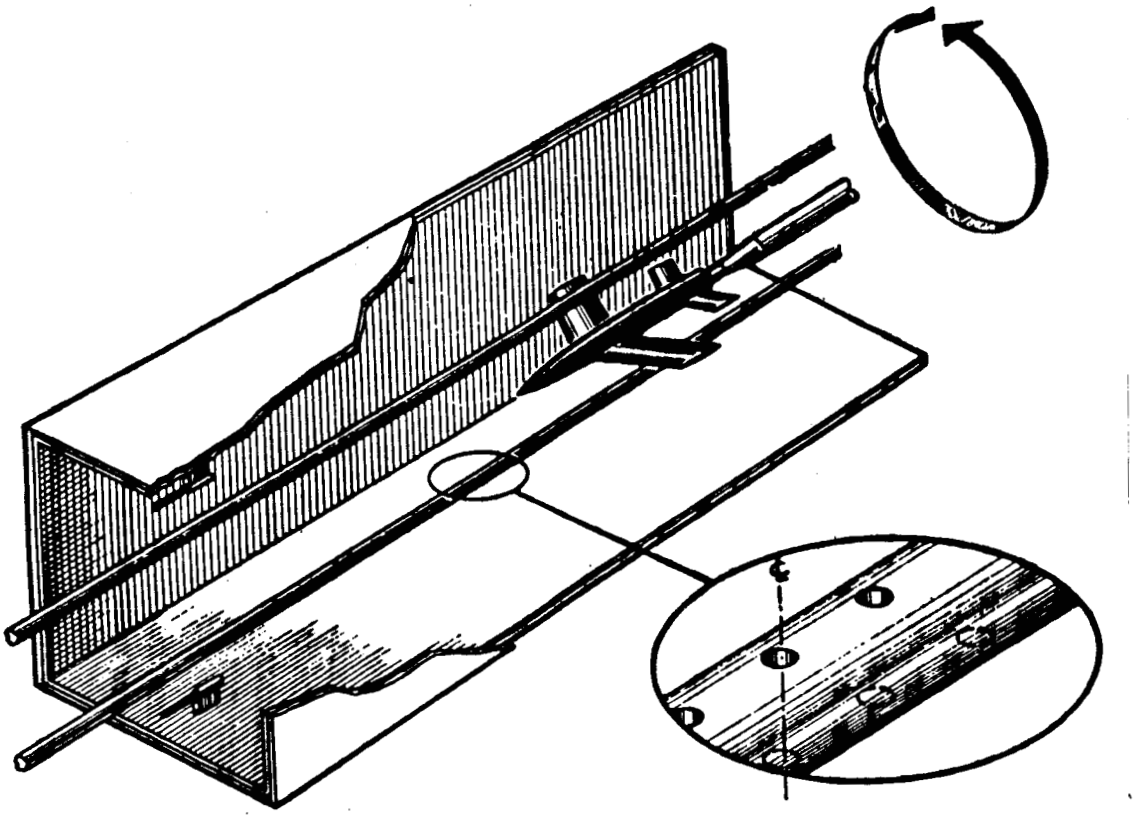

Figure 3. Calspan Pipe: Velocity Measurement System.

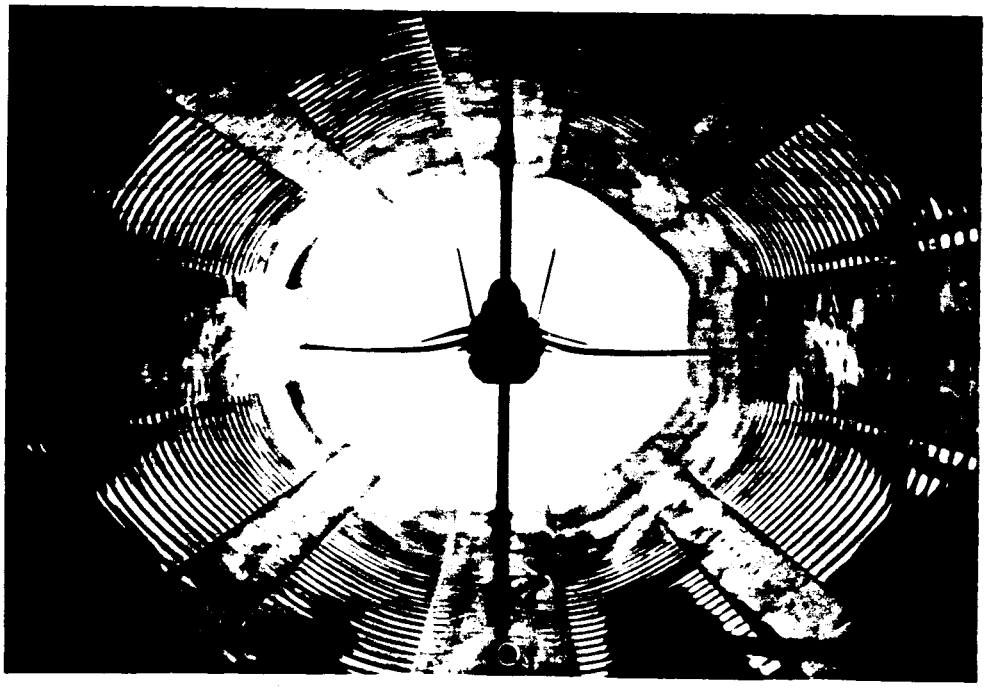

Figure 4. Octagon Test Section with Canard Model.

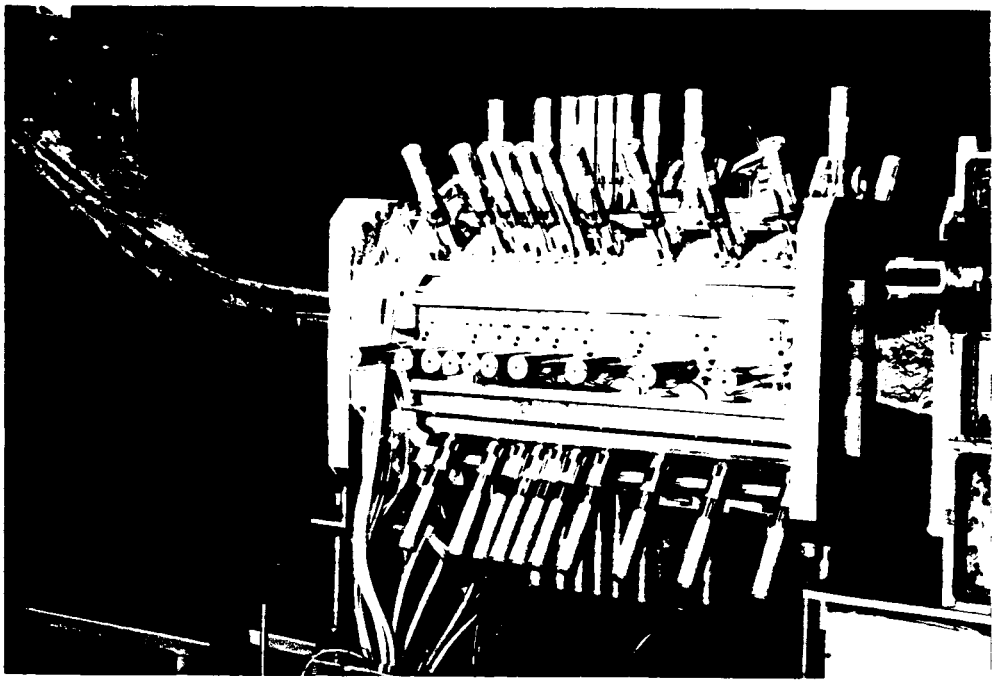

Figure 5. External View of the Octagon Test Section.

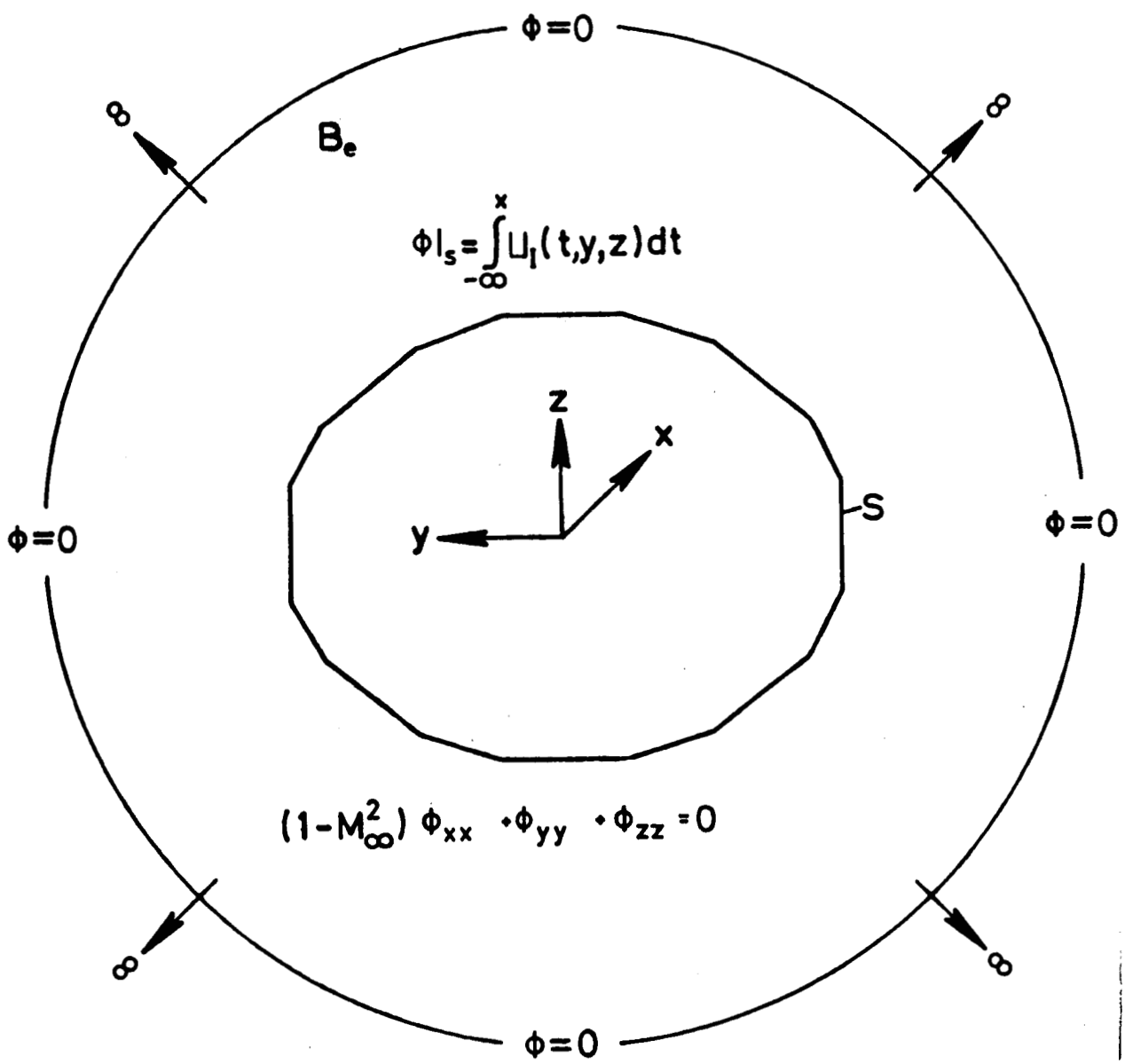

Figure 6. Three-Dimensional Design Task in the Subsonic Case.

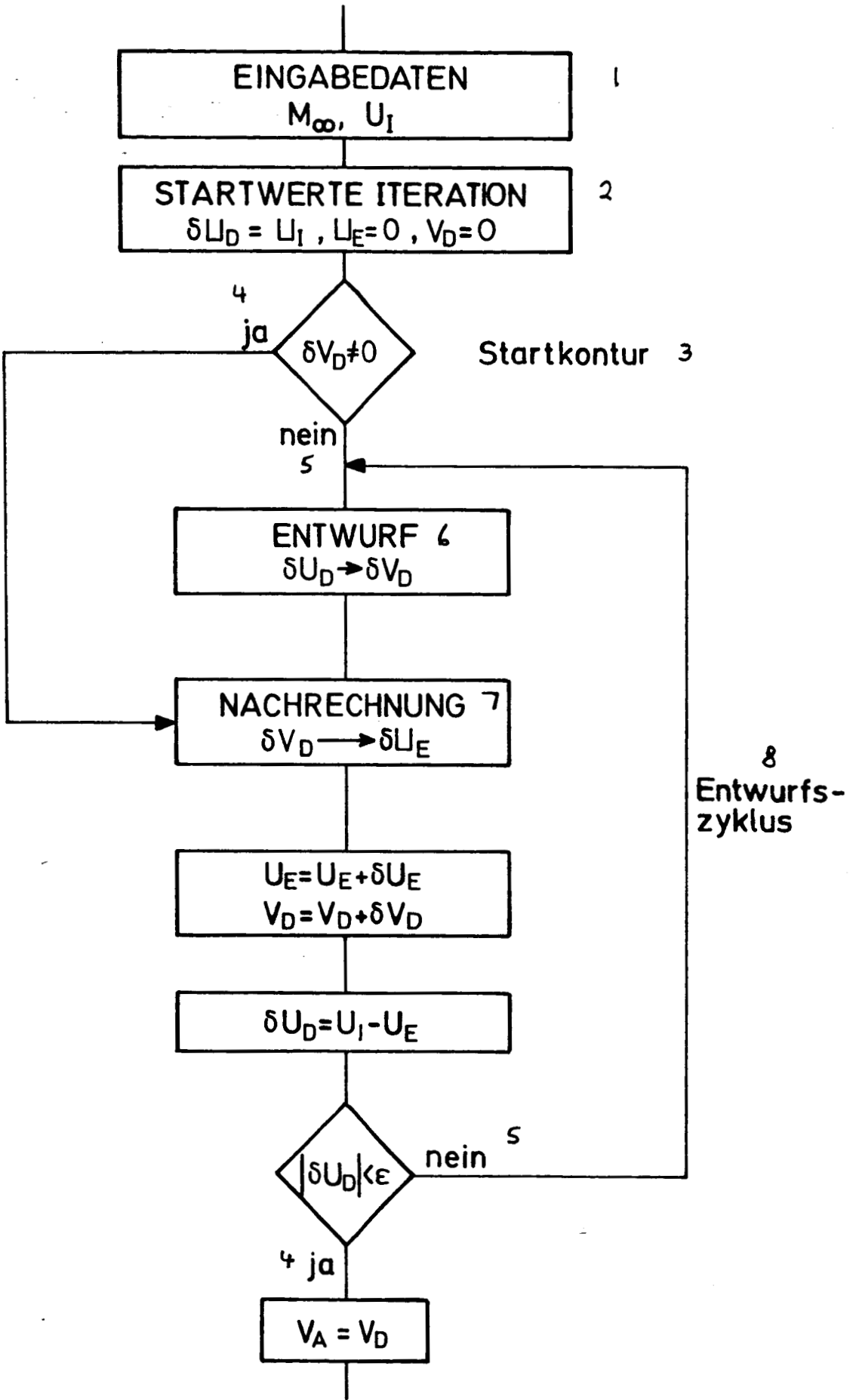

Figure 7. Design Methods.

Key: 1) input data; 2) iteration starting values; 3) initial contour; 4) yes; 5) no; 6) design; 7) post calculation; 8) design cycle.

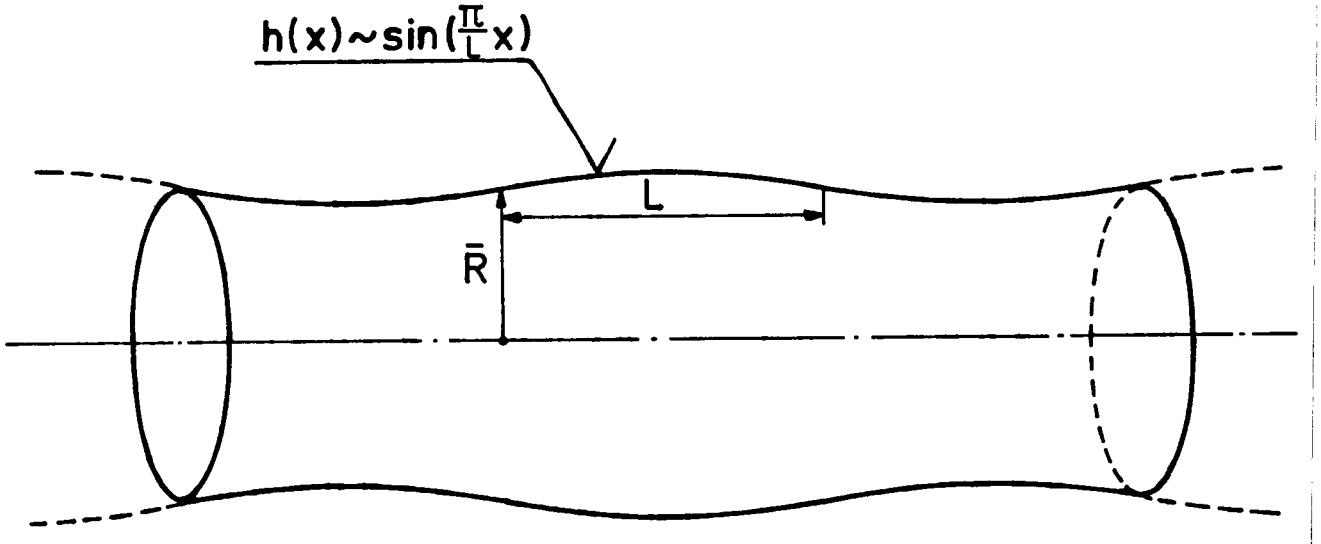

$$V_D' = \frac{1}{\bar{R}\ln\left(\frac{\pi\bar{R}}{L}\sqrt{1-M_\infty^2}\right)} U_D , \quad M_\infty<1$$

Figure 8. Design Rule.

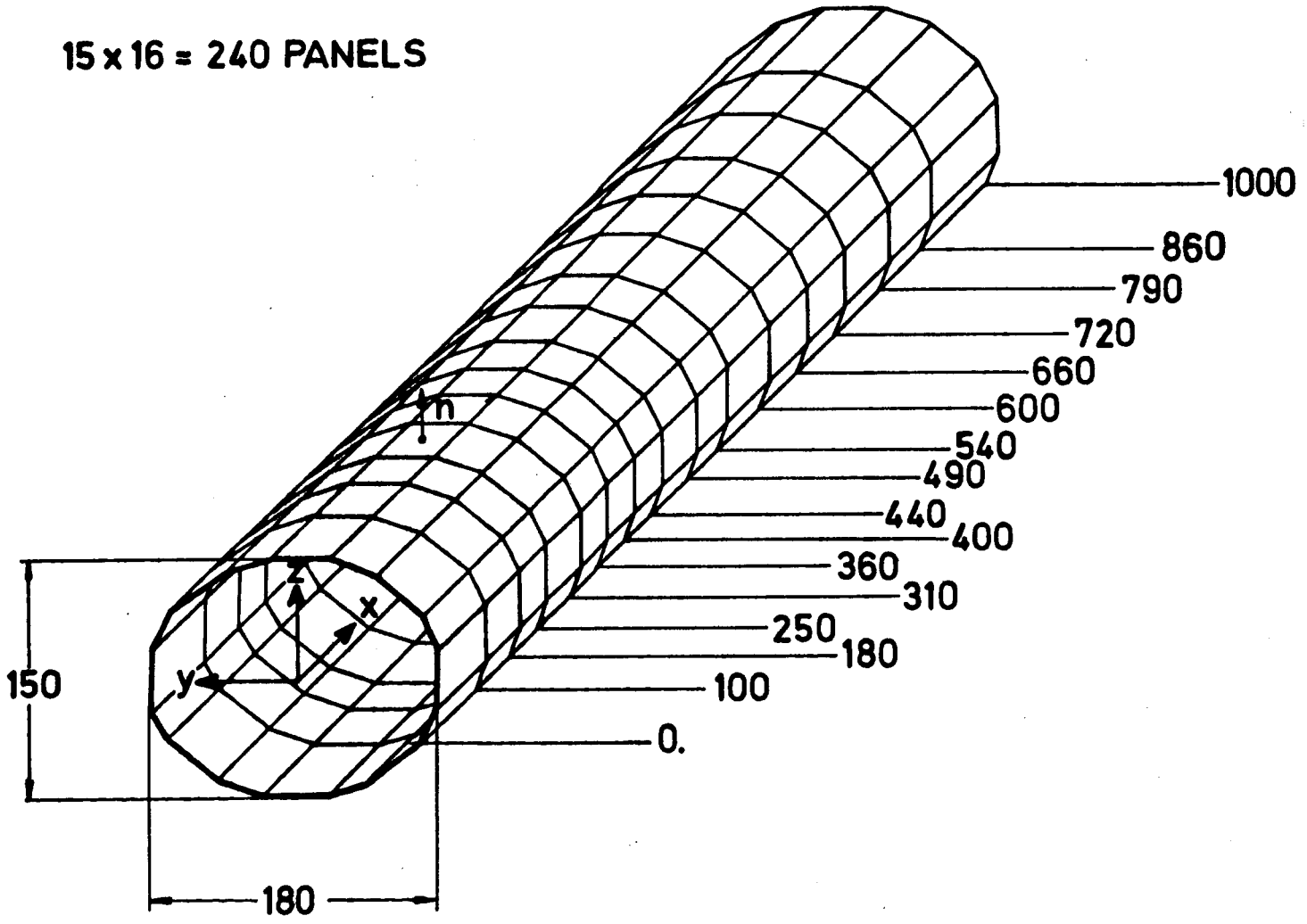

Figure 9. Paneling of Control Surface.

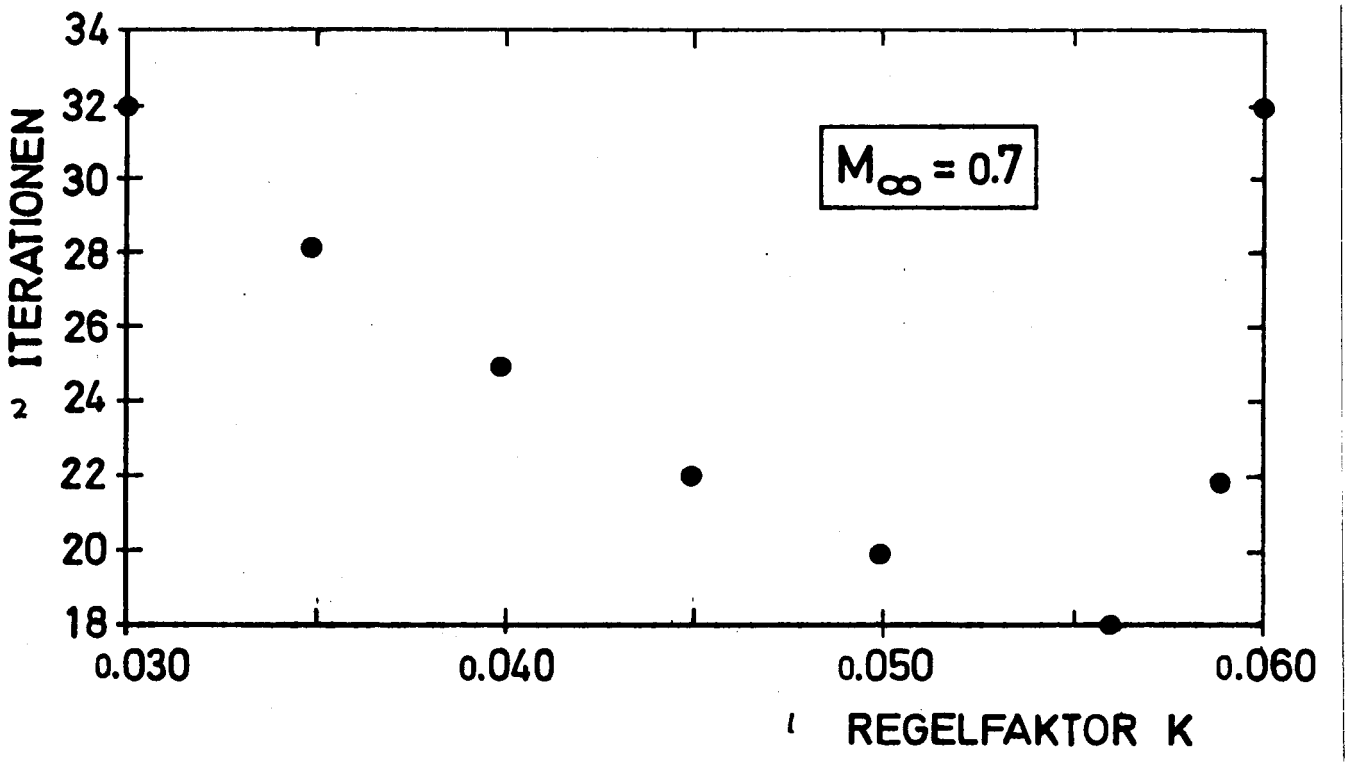

Figure 10. Convergence of Iteration Wall Adaptation.
Key: 1) regulation factor K; 2) iterations.

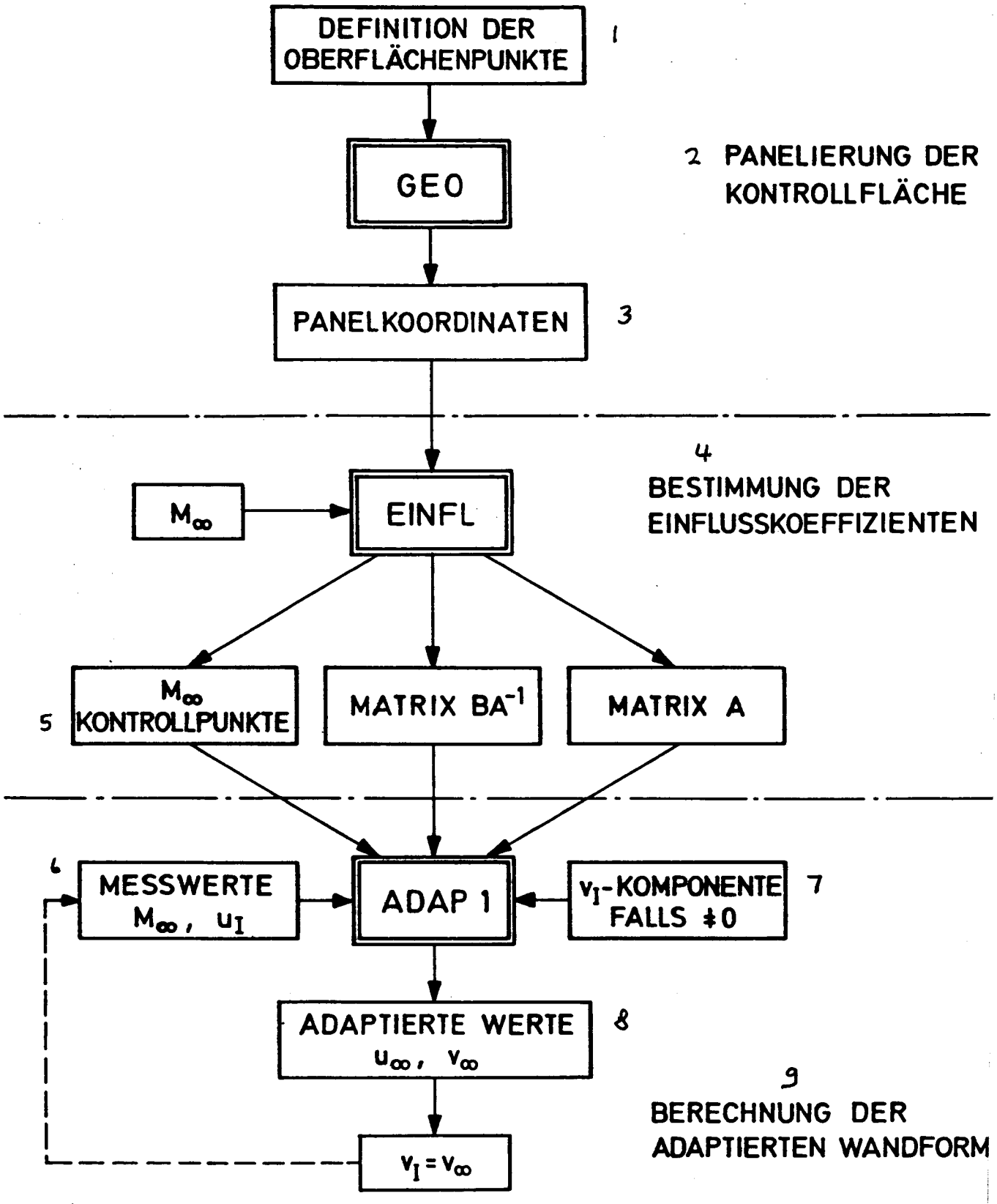

Figure 11. Subsonic Programming System.

Key: 1) definition of surface points; 2) paneling of control surface; 3) panel coordinates; 4) determination of influence coefficients; 5) control points; 6) measured values; 7) component if; 8) adapted values; 9) calculation of the adapted wall shape.

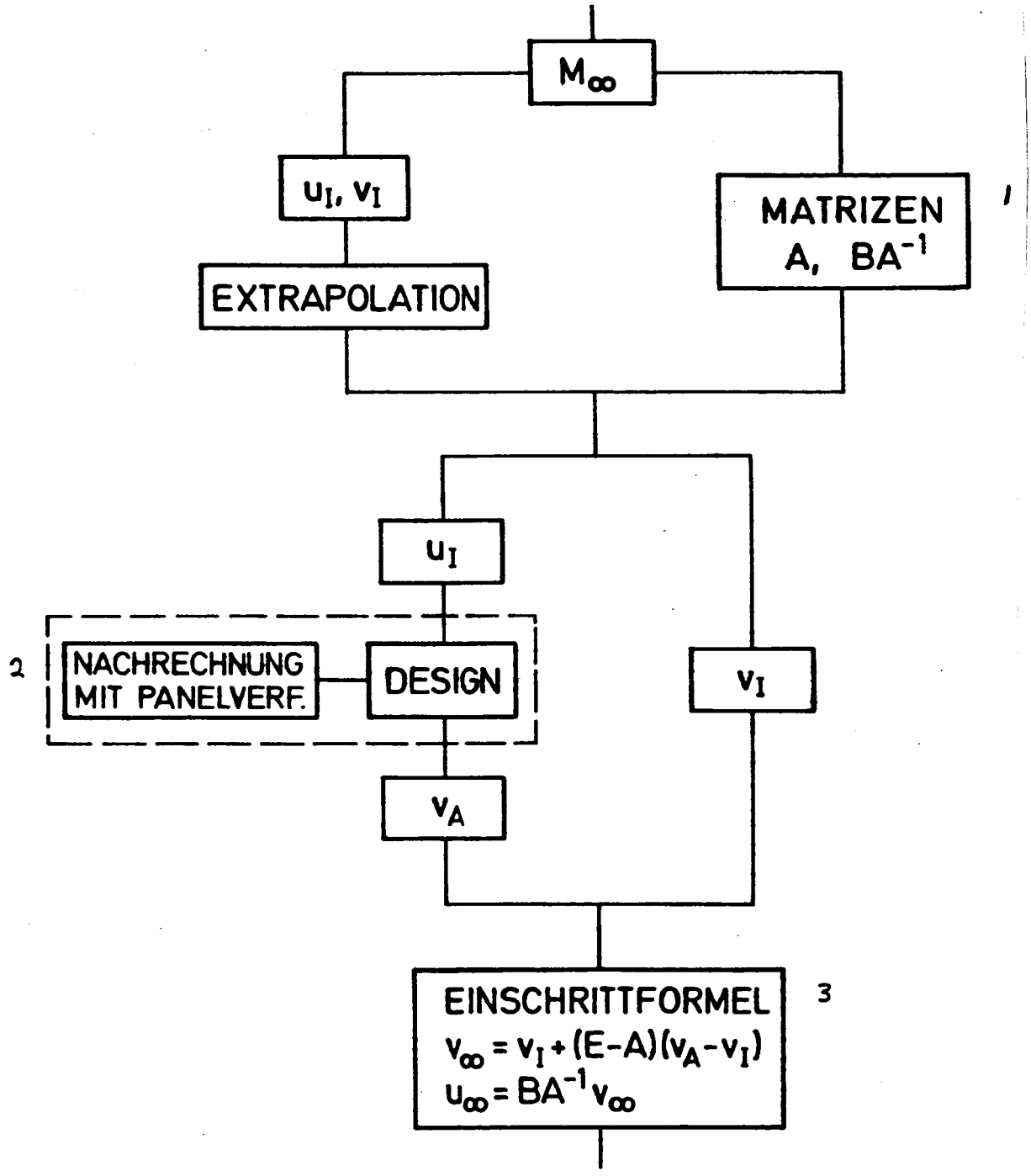

Figure 12. Adaptation Program ADAP 1.

Key: 1) matrices; 2) post calculation with panel method; 3) single step formula.

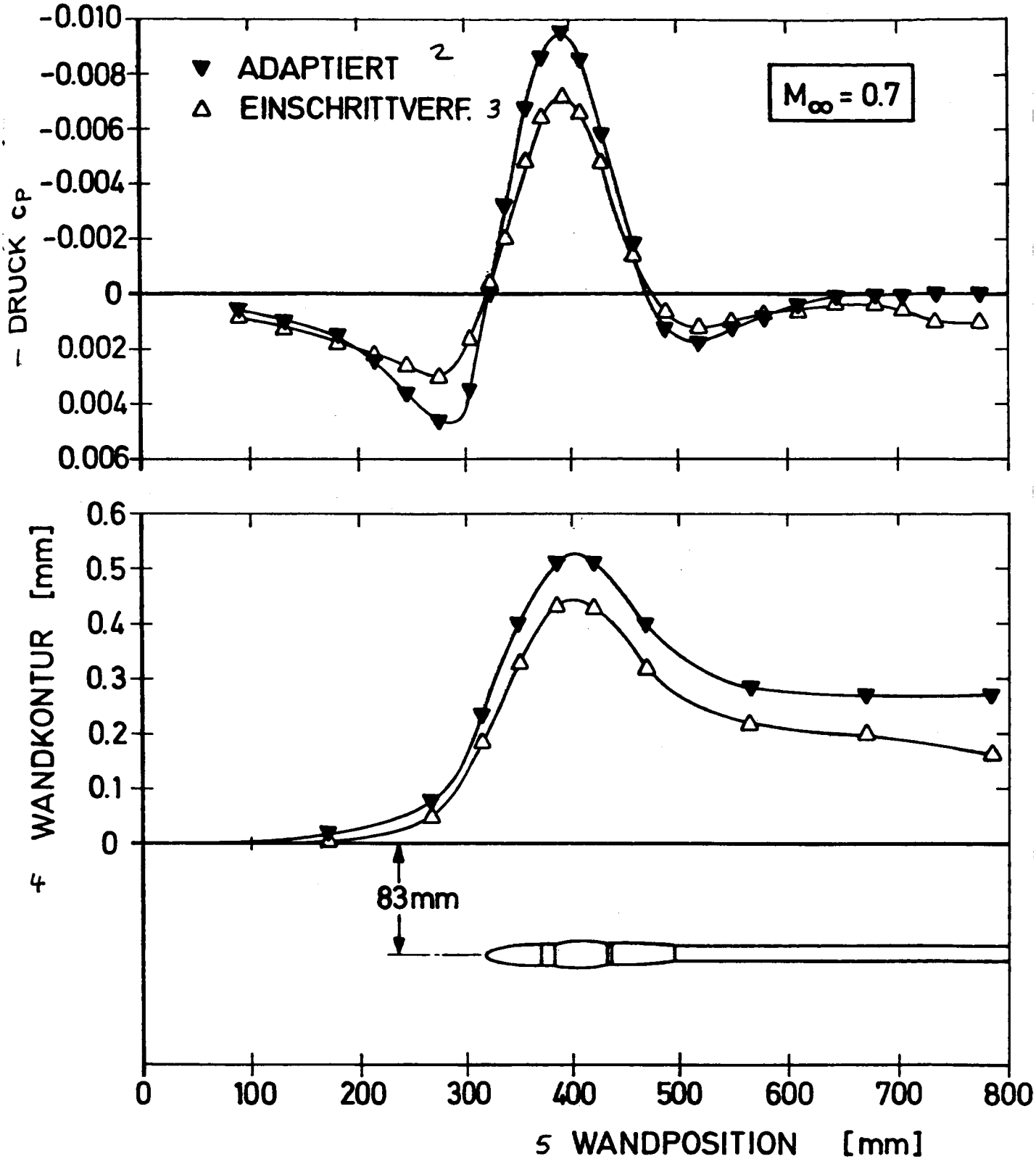

Figure 13. Analytical Test Case C5-Body.

Key: 1) pressure; 2) adaptive; 3) single step method; 4) wall contour; 5) wall position.

C-2

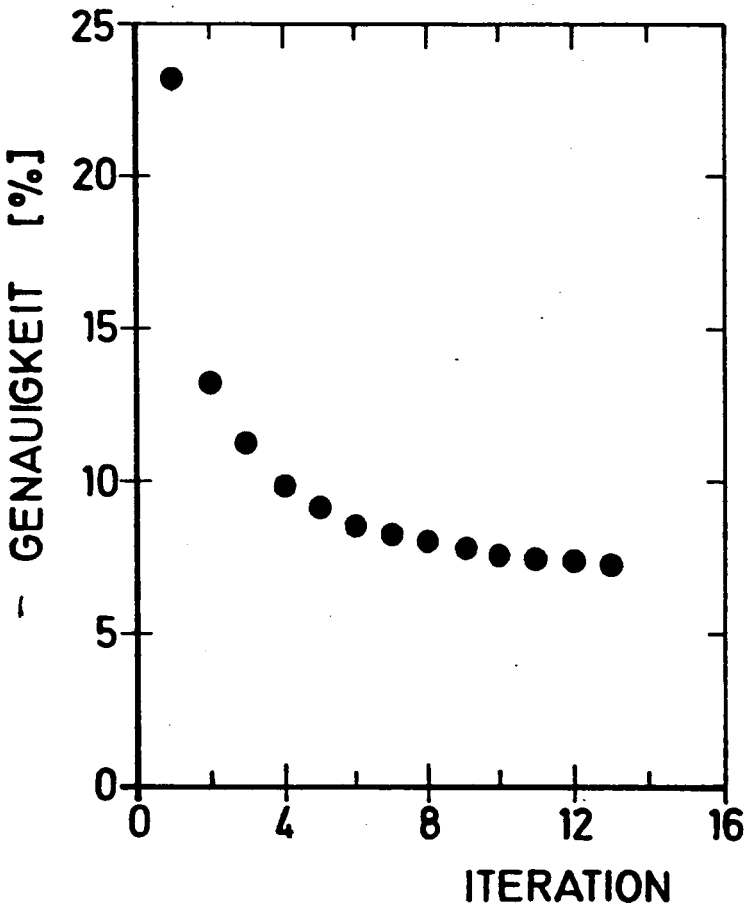

Figure 14. Convergence of Design Method.
Key: 1) accuracy.

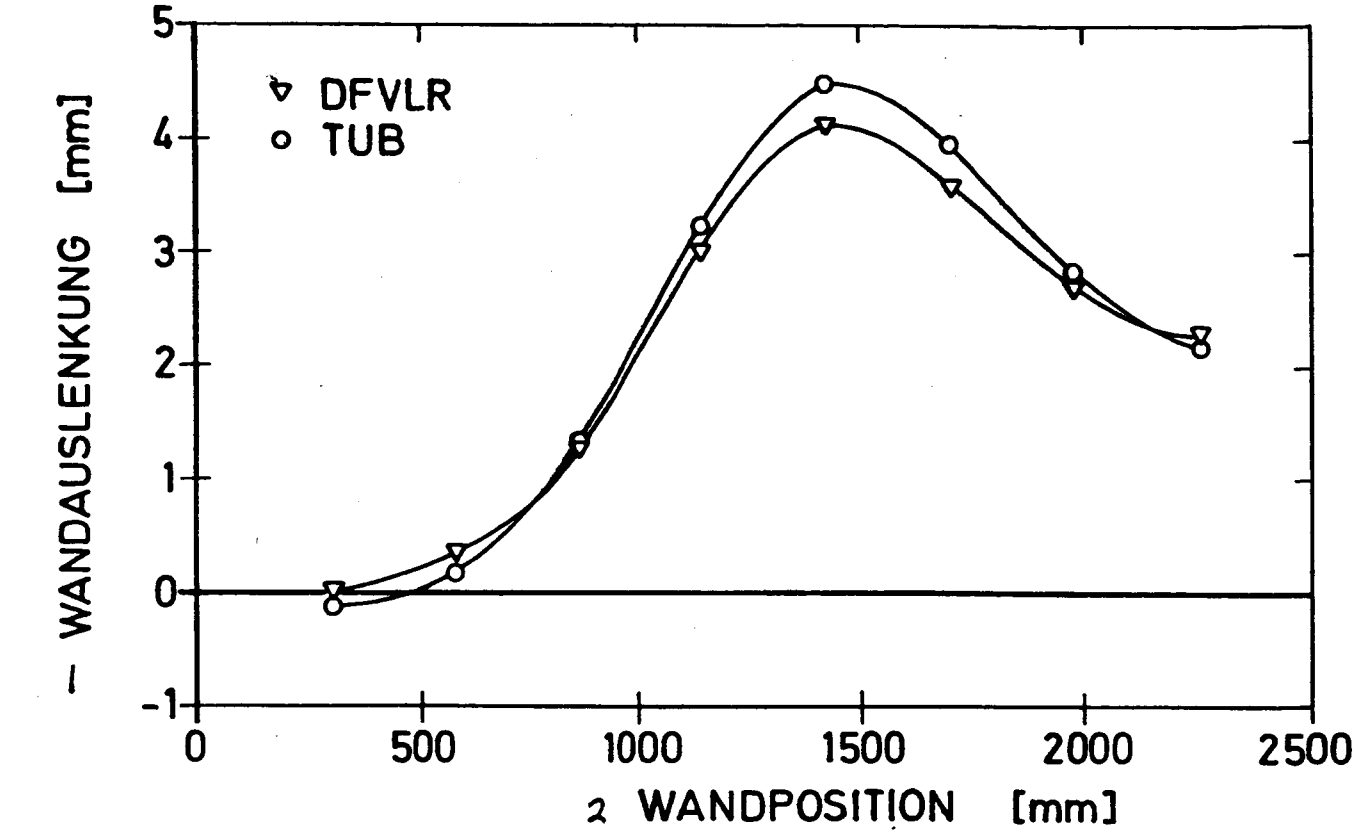

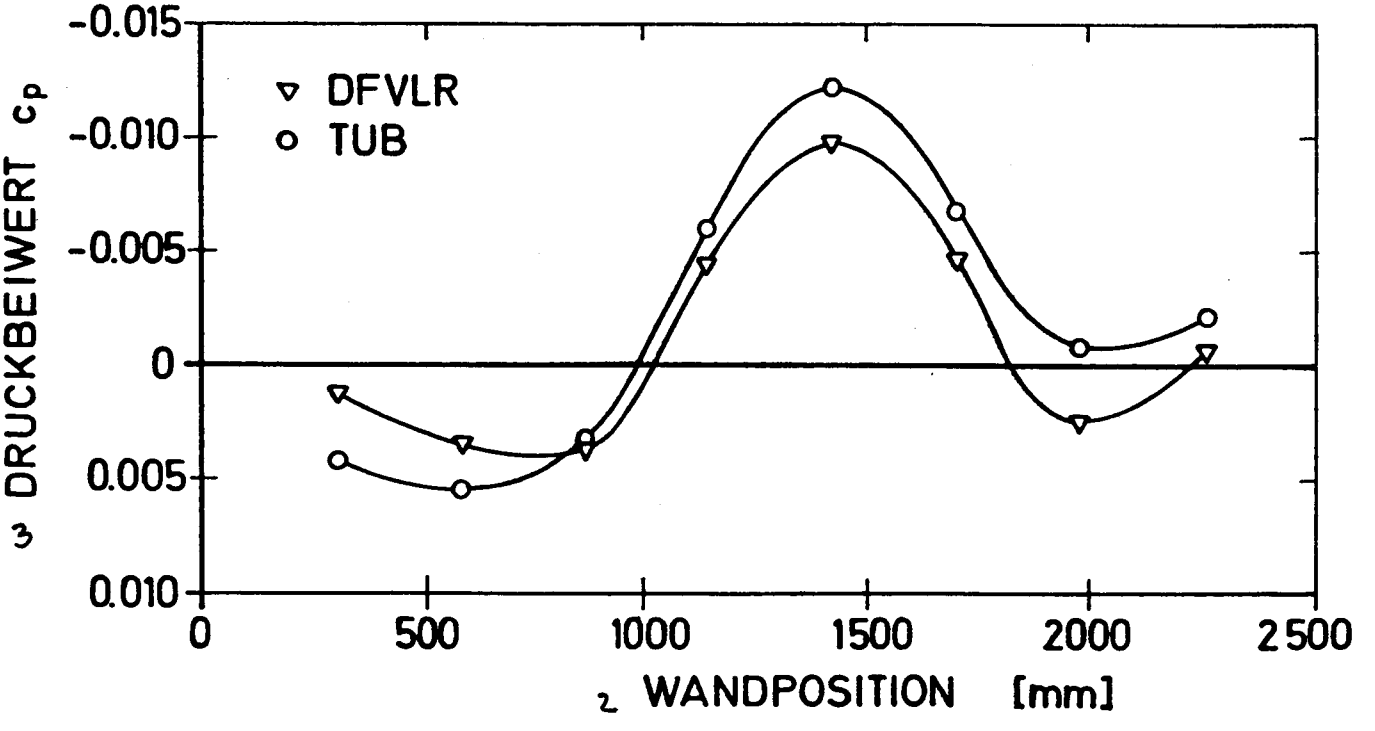

Figure 15a. FFA-Model.

Key: 1) wall deflection; 2) wall position; 3) pressure coefficients.

$M_\infty = 0.4994 \quad (M_{kor} = 0.5036) \quad \alpha = 0°$

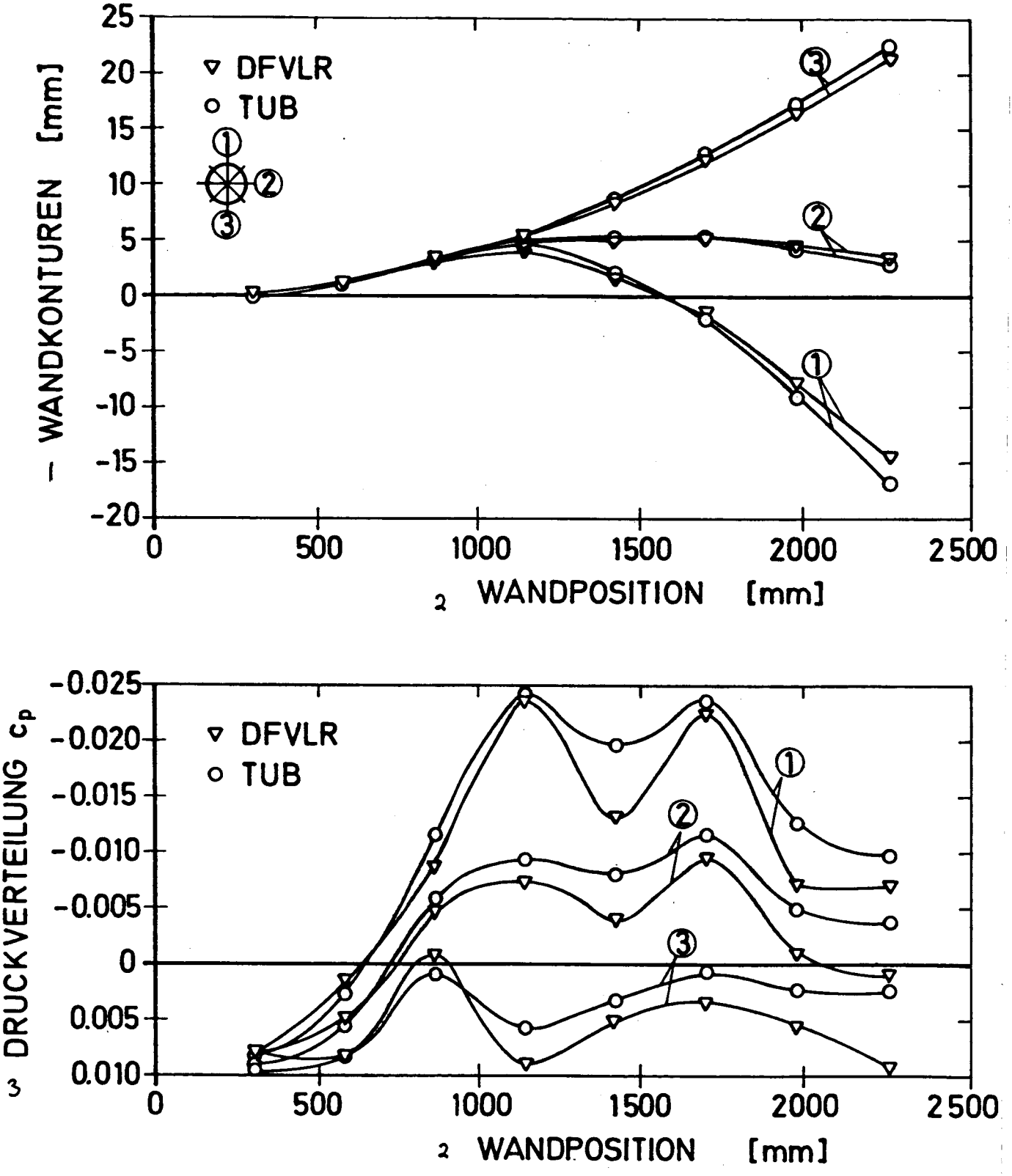

Figure 15b. AGB-Model 3.5%.

Key: 1) wall contours; 2) wall position; 3) pressure distribution.

$$M_\infty = 0.4998 \qquad (M_{kor} = 0.5060) \qquad \alpha = 4°$$

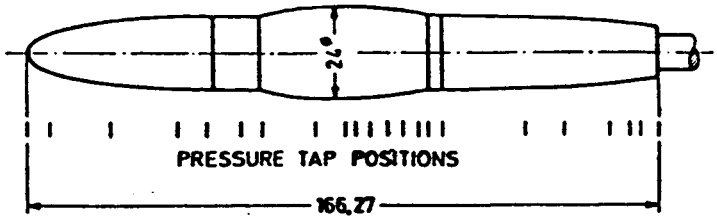

Figure 16. a) Onera Calibration Model C5.

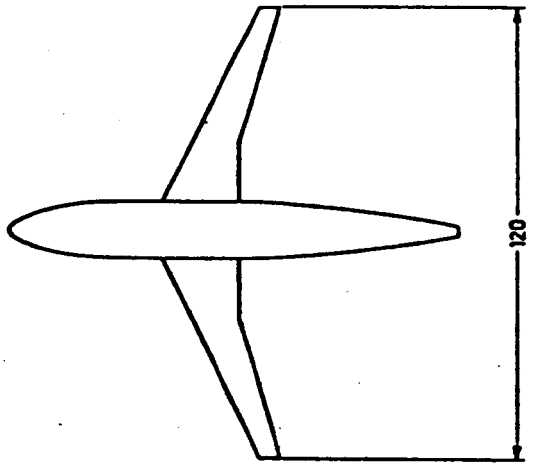

b) ZKP F4-Model.

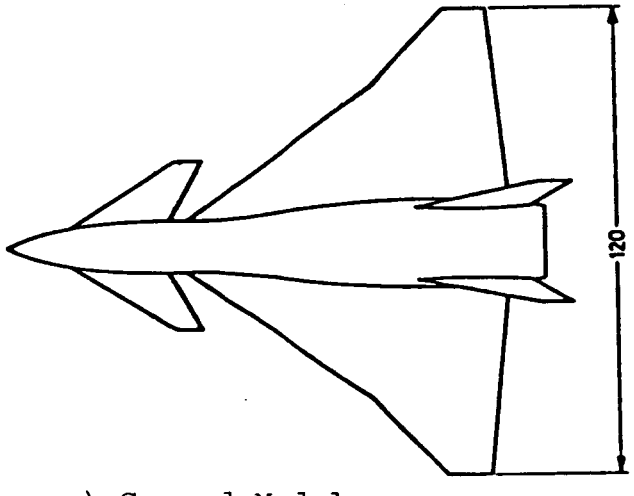

c) Canard Model.

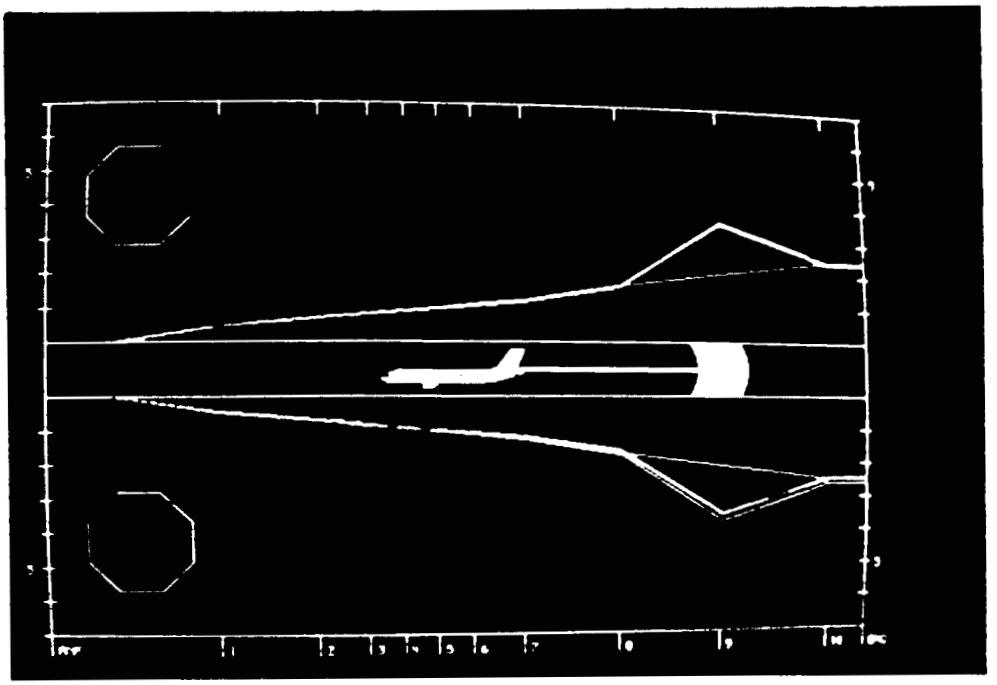

Figure 17. Preliminary Adjustment of Walls (M_∞ = 0.8).

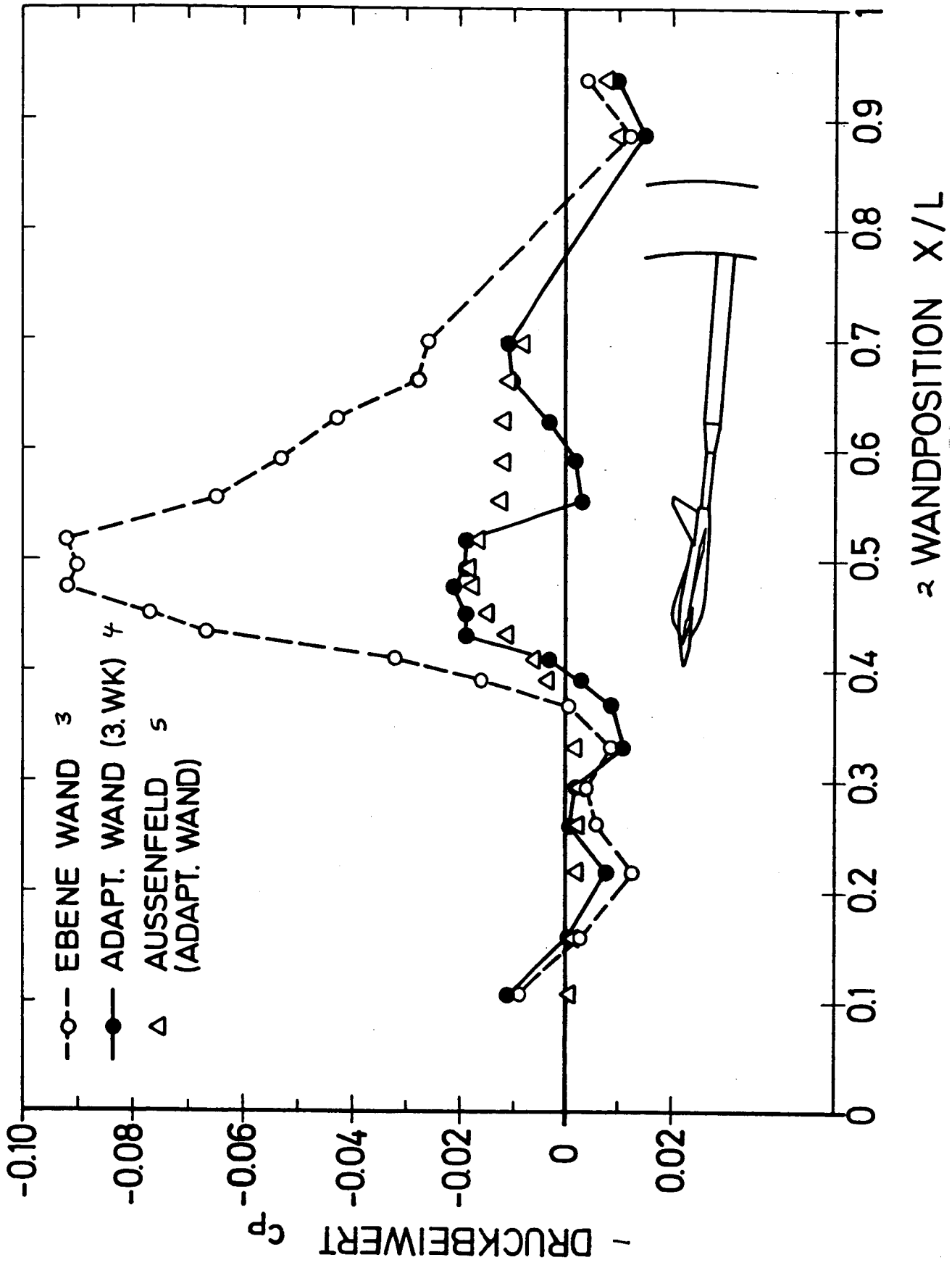

Figure 18. Canard Model.

Key: 1) pressure coefficient; 2) wall position; 3) flat wall; 4) adapted wall (3rd WK); 5) outer field (adapted wall).

$M_\infty = 0.7 \qquad \alpha = 4.54°$

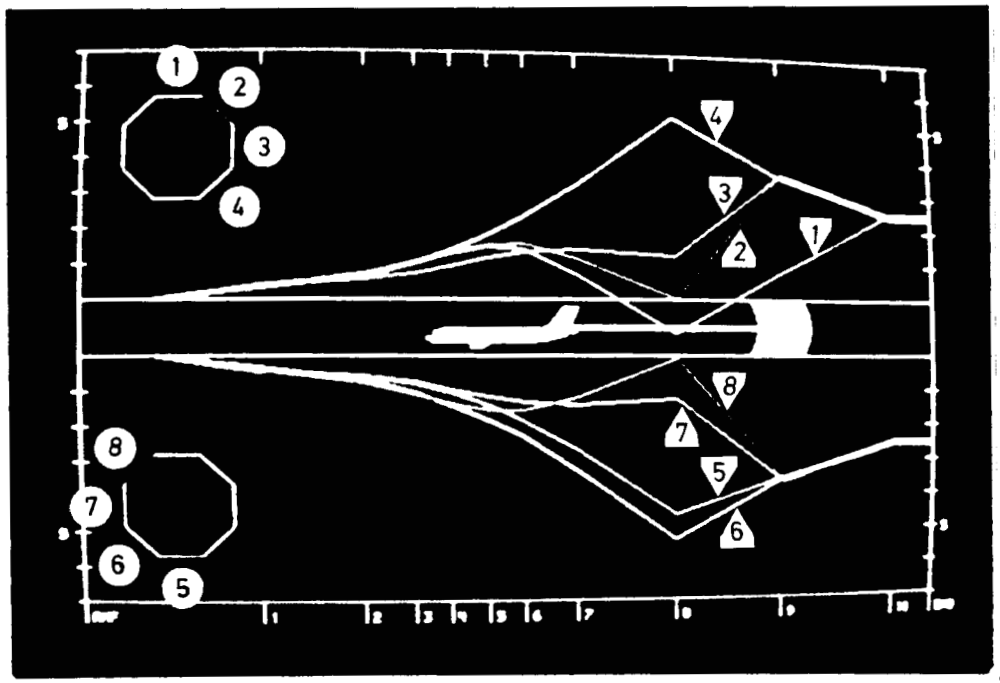

Figure 19. Adaptive Wall Contour, Canard Model. M_∞ = 0.8, α = 8.04

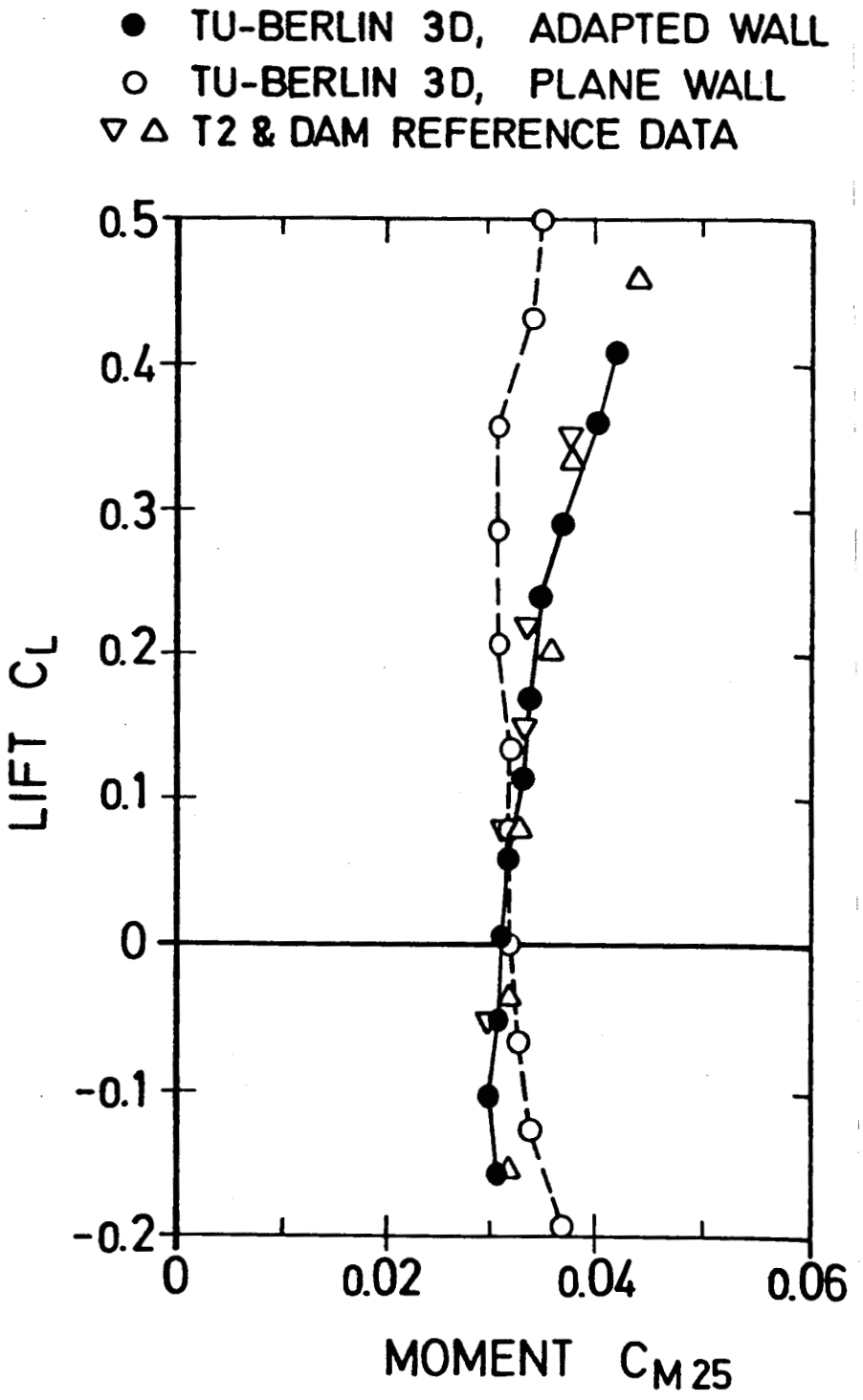

Figure 20. Canard Model.

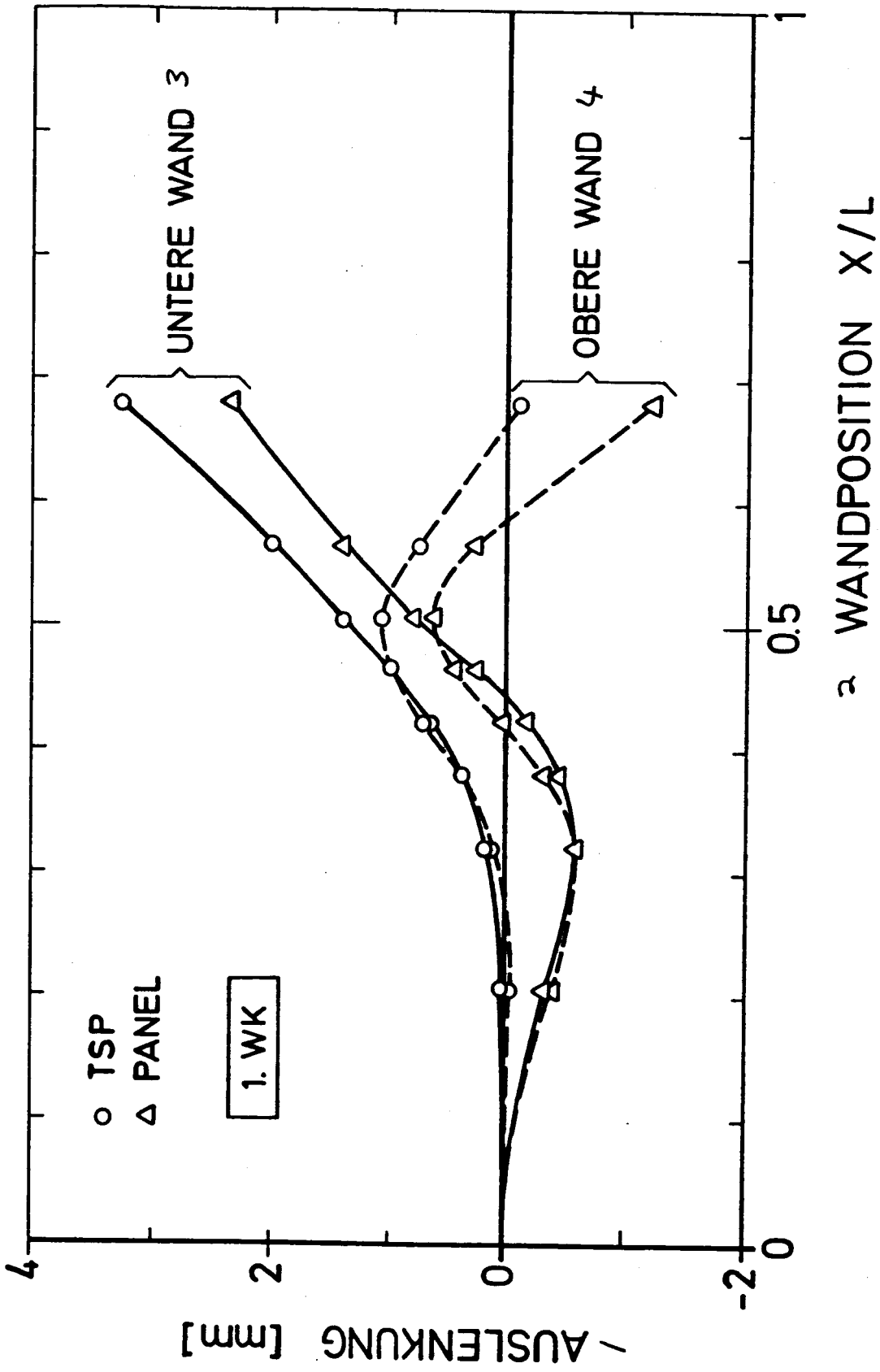

Figure 21. Canard Model.

Key: 1) deflection; 2) wall position; 3) lower wall; 4) upper wall.

$M_\infty = 0.95; \quad \alpha = 3.61°$

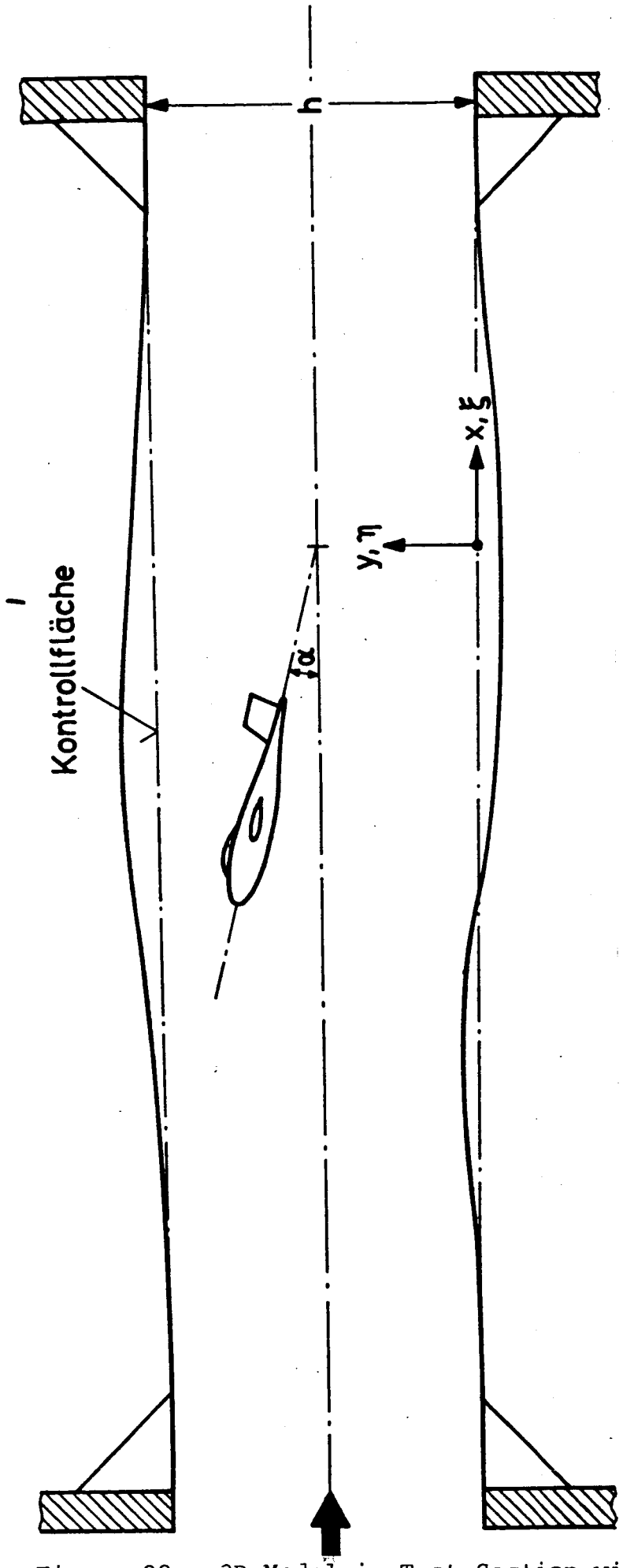

Figure 22. 3D-Model in Test Section with Two Flexible Walls.

Key: 1) control surface.

POSTSCRIPT

This work was done during my activity as a scientific worker at the Institute for Aerodynamics in Space Flight at the Technical University Berlin.

I would like to thank Professor Ganzer for scientific advice and his interest during the writing of the paper.

I was stimulated by Professor Renner and Barche and thank them for carrying out my examination.

I would like to thank the members of the working group of Professor Ganzer for their collaboration and the friendly working atmosphere.

VITAE

Rainer Rebstock

born [redacted] in [redacted]

1960 - 1964	Lower schools
1964 - 1972	Mathematical natural gymnasium
May 1982	Abitur
After Winter Semester 72/73	Study of Mathematics and Physics at the TU Berlin
May 1975	Preliminary Diploma Examination
October 1979	Diploma
November 1979 - March 1986	Scientific employee at the Institute for Aerodynamics and Space Flight at the TU Berlin